

1 Quantifying Temperature-sliding Inconsistency in Thermomechanical Coupling: A
2 Comparative Analysis of Geothermal Heat Flux Datasets at Totten Glacier

3
4 Junshun Wang¹, Liyun Zhao¹, Michael Wolovick^{2,3}, John C. Moore⁴

5 ¹State Key Laboratory of Earth Surface Processes and Hazards Risk Governance
6 (ESPHR), Faculty of Geographical Science, Beijing Normal University, Beijing
7 100875, China

8 ²Center for Industrial Mathematics (ZeTeM), University of Bremen, Bremen, Germany

9 ³Glaciology Section, Alfred-Wegener-Institut, Helmholtz-Zentrum für Polar- und
10 Meeresforschung, Bremerhaven, Germany

11 ⁴Arctic Centre, University of Lapland, Rovaniemi, Finland

12 *Correspondence: Liyun Zhao (zhaoliyun@bnu.edu.cn), John C. Moore*
13 *(john.moore.bnu@gmail.com)*

14
15
16
17 **Abstract.** Rapid sliding of ice sheets requires warm basal temperatures and lubricating
18 basal meltwater, whereas slow velocities typically correlate with a frozen bed. However,
19 ice sheet models often infer basal sliding by inverting surface velocity observations
20 with the vertical structure of temperature and hence rheology held constant. If the
21 inversion is allowed to freely vary sliding over the model domain, then inconsistencies
22 between the basal thermal state and ice motion can arise lowering simulation realism.
23 In this study, we propose a new method that quantifies inconsistencies when inferring
24 thawed and frozen-bedded regions of ice sheets. This method can be used to evaluate
25 the quality of ice sheet simulation results without requiring any englacial or subglacial
26 measurements. We apply the method to evaluate simulation results for Totten Glacier
27 using an isotropic 3D full-Stokes ice sheet model with eight geothermal heat flux (GHF)
28 datasets and compare our evaluation results with inferences on basal thermal state from
29 radar specularity. The rankings of GHF datasets based on inconsistency are closely
30 aligned with those using the independent specularity content data. ~~Examples of To~~
31 ~~illustrate~~ the ~~method~~method's utility ~~are 1~~, we identified an overcooling inconsistency
32 ~~with~~across all GHFs near the western boundary of Totten Glacier ~~between~~(70°S-72°S;
33 ~~where there is~~), a region with a bedrock canyon and fast surface ice velocities,
34 suggesting that all GHFs are ~~low~~; 2. underestimated. Conversely, an overheating
35 inconsistency ~~exists~~ in ~~the~~ eastern Totten Glacier ~~with~~across all GHFs ~~suggesting~~,
36 ~~indicating an~~ overestimation of ice temperature ~~due~~that, in this case, ~~to~~is associated
37 ~~with~~ a warm bias in ~~the~~ surface temperature. Our approach opens a new avenue for

38 assessing the self-consistency and reliability of ice sheet model results and GHF
39 datasets, which may be widely applicable.

41 1. Introduction

42 Ice sheet models are an important tool for projections of ice sheet mass balance
43 and their contribution to sea level rise. Ice sheet models are usually initialized by “spin-
44 up” or data assimilation such that they reproduce the present-day geometry or surface
45 velocity of an ice sheet (Seroussi et al., 2019). Often ice sheet model simulations derive
46 ice dynamics using ice temperatures taken from other studies (e.g., Gillet-Chaulet et al.,
47 2012; Cornford et al., 2015; Pittard et al., 2016; Siahayan et al., 2022). In thermo-
48 mechanically coupled ice sheet simulations, the ice sheet model is usually spun up with
49 idealized temperature-depth profiles and then run in a thermo-mechanically coupled
50 mode constrained by geothermal heat flux (GHF) and surface ice temperature fields
51 (Seroussi et al., 2019). While advances in satellite and field observation technologies
52 have led to a preliminary consensus on ice sheet geometry and surface ice temperature,
53 significant uncertainties persist in basal boundary conditions, including GHF and basal
54 friction, since reliable observational data are scarce. These basal properties introduce
55 significant uncertainty in the simulated ice sheet dynamics, and thus ice sheet mass
56 balance.

57 The GHF, the heat flow from the Earth's crust to the base of ice sheet, is a critical
58 variable in the basal boundary condition for simulating the ice temperature profile, and
59 hence ice rheology and flow dynamics (Fisher et al., 2015; Smith - Johnsen et al., 2020;
60 Reading et al., 2022). Several GHF datasets exist, derived in various ways from
61 geophysical observations and models, and they exhibit significant variability in both
62 spatial distribution and magnitude (e.g., An et al., 2015; Dziadek et al., 2017; Martos et
63 al., 2017; Shen et al., 2020; Stål et al., 2021). These GHF datasets have been widely
64 used in thermodynamic simulations of Antarctica (e.g., McCormack et al., 2022;
65 Shackleton et al., 2023; Park et al., 2024; Van Liefferinge et al., 2018). However,
66 assessing the GHF field accuracy is problematic because in situ measurements such as
67 boreholes are sparse. Few studies have assessed the quality and reliability of GHF
68 datasets over specific regions. Kang et al. (2022) employed a combination of forward
69 model and inversion using a 3D full-Stokes ice flow model to simulate the basal thermal
70 state in the Lambert–Amery Glacier region and evaluate different GHFs using the
71 locations of subglacial lakes, but the constraints used were asymmetric between frozen
72 and thawed beds, and assigned inflated reliability to the warmer GHF maps. Indirect
73 estimates of basal conditions have used airborne radar specular content (Schroeder
74 et al., 2013, 2015; Young et al., 2016) as proxies for basal wetness/dryness and thermal
75 regime (Dow et al., 2020). Huang et al. (2024) used an inverse modeling approach
76 similar to that of Kang et al. (2022) for Totten Glacier and combined this with measured

77 radar specularity content to derive a two-sided constraint on the basal thermal state in
78 addition to subglacial lakes locations. However, specularity content is not yet available
79 for many regions of Antarctica.

80 The basal friction field is another poorly known boundary condition in ice sheet
81 modeling, and a key source of uncertainty in the long-term projection of ice sheets and
82 glaciers. Although basal slip is crucial to the 3D ice flow, it is difficult to observe.
83 Several basal sliding parameterizations have been proposed and widely used
84 (Weertman, 1957; Kamb, 1970; Nye, 1970; Budd et al., 1979; Fowler, 1981; Schoof,
85 2005; Gagliardini et al., 2007; Gladstone et al., 2014; Tsai et al., 2015; Brondex et al.,
86 2017, 2019). The linear Weertman basal sliding parameterization is the most widely
87 used due to its simple form. Given prescribed or modelled ice temperatures and hence
88 ice viscosity, numerous studies have inferred the spatial distribution of the basal friction
89 coefficient over grounded ice to best match observed present-day surface ice velocities
90 or ice sheet geometry using snapshot or time-dependent data assimilation and inverse
91 methods (MacAyeal, 1993; Gillet-Chaulet et al., 2012; Larour et al., 2012; Pollard and
92 DeConto, 2012; Morlighem et al., 2013; Pattyn, 2017; Albrecht et al., 2020; Lipscomb
93 et al., 2021; Choi et al., 2023). However, such inversions typically allow the friction
94 coefficient to vary freely to match the surface velocity observations. This can
95 potentially lead to conflicts with the temperature field used during the inversion. For
96 instance, relatively fast surface ice velocity may demand basal sliding in areas where
97 the basal temperatures are below the local pressure melting point. However, many
98 studies overlook this aspect, and use the inversion results to initialize ice sheet
99 dynamics simulations and estimate glacier mass balance and its contribution to sea level
100 rise (Seroussi et al., 2019; Peyaud et al., 2020; Schannwell et al., 2020; Payne et al.,
101 2021).

102 For this study, we define the inconsistencies as differences between a sliding
103 inversion and the temperature/rheology field used as an input to that inversion. More
104 specifically, the inconsistencies are between modelled basal sliding (which is tuned to
105 match the observed fast surface velocity during the inversion) and modelled frozen bed,
106 and between observed slow surface velocity (which is most likely indicative of a non-
107 slip basal condition) and modelled thawed bed. The inconsistencies originate from
108 multiple causes, including uncertainties in GHF, surface ice temperature, ice sheet
109 geometry, bed topography, surface velocity, ice density and incomplete ice flow
110 mechanics.

111 To the best of our knowledge, there has been no study of such inconsistencies.
112 Here we develop a novel and generally applicable method to estimate this inconsistency
113 without relying on basal observation data. We utilize this approach to evaluate the
114 quality of ice flow model results. Notably, this approach can also serve as a

115 supplementary method for assessing geothermal heat flux datasets, relying solely on
116 surface ice velocity observations rather than additional englacial or subglacial data.

117 We apply our method to Totten Glacier, a primary outlet of the Aurora subglacial
118 basin in East Antarctica (Greenbaum et al., 2015; Pritchard et al., 2009). The Totten
119 Glacier subregion experienced the largest mass loss among drainage basins in East
120 Antarctica during the period 1979-2017 and 2003-2020 (Kim et al., 2024; Rignot et al.,
121 2019) (Fig. 1a). We examine inconsistencies between simulated ice temperature and ice
122 velocity fields from Huang et al. (2024) using a 3D full-Stokes model with the various
123 GHFs, and we use this analysis to rank the reliability of different GHF fields. This GHF
124 ranking closely resembles that reported by Huang et al. (2024), which used the
125 agreement between the modelled basal thermal regime and specularly content, which
126 we take as a validation of the method. Since the new method does not require any
127 englacial or subglacial data, it can be applied to many glaciers, particularly those
128 lacking observations. Our approach can provide a swift assessment of the plausibility
129 of basal temperature and velocity simulated by ice sheet models. Additionally, it can be
130 effectively utilized to map the spatial distribution of GHF over- or under-estimation.

131

132 **2. Method**

133 **2.1 Methodology in this study**

134 **2.1.1 Definition of Metrics**

135 There is no direct correlation between basal temperature and surface velocity;
136 rather, they are linked through the basal thermal state - the basal temperature being at
137 or below the pressure melting point. The ice bottom in the study domain can be
138 partitioned into thawed and frozen beds depending on whether the simulated basal ice
139 temperature reaches the local pressure melting point. To effectively penalize models
140 exhibiting both localized overheating (bed too warm) and overcooling (bed too cold),
141 we establish overheating metrics within the thawed-bedded region and overcooling
142 metrics within the frozen-bedded region to quantitatively assess the inconsistency
143 between the simulated temperature and velocity fields. Thus, we provide two-sided
144 constraints on the temperature field that penalize both too high and too low ice
145 temperature.

146 Overcooling occurs where basal temperature is underestimated. Crucially, in
147 regions with relatively fast observed surface velocity, the inverse method nevertheless
148 yields a nonzero basal velocity — a physically inconsistent result given the cold basal
149 temperature. When basal ice temperature is below the pressure melting point, the basal
150 modelled velocity is expected to approach zero. This inconsistency is larger for faster
151 simulated basal velocity magnitude and for colder simulated basal temperatures. We
152 therefore use a formula that accounts for both variables to quantify overcooling:

$$153 \quad AOC = (T_{melt} - T_{bm}) \times U_{bm}, \quad (1)$$

154 where AOC stands for absolute overcooling, T_{melt} is the basal pressure melting point,
 155 T_{bm} represents the simulated basal ice temperature and U_{bm} means the simulated basal
 156 velocity magnitude.

157 It is not straightforward to quantify the inconsistencies between modelled thawed
 158 bed and expected slow basal velocity magnitude given slow observed surface velocity
 159 magnitude. We note the fact that modelled basal sliding velocity magnitude must
 160 remain non-negative. If the ice is warm and soft enough to permit deformation such
 161 that the modelled surface velocity magnitude is much faster than the observed, then a
 162 friction inversion will be ineffective to correct this misfit, producing a bias towards
 163 positive misfits (i.e., model velocities are too fast) in the inversion results. Therefore,
 164 we use the positive difference between simulated and observed surface velocity
 165 magnitude to calculate the inconsistency caused by the overheating effect:

$$166 \quad AOH = \max(0, U_{sm} - U_{obs}), \quad (2)$$

167 where AOH refers to absolute overheating, U_{sm} represents the modelled surface
 168 velocity magnitude and U_{obs} is the observed surface velocity magnitude. We only
 169 calculated AOH for the thawed-bedded areas, i.e. $T_{bm} = T_{melt}$, because observed surface
 170 velocity magnitude errors are proportionally much less in thawed-bedded areas
 171 (corresponding to fast flow regions) than in frozen-bedded area (correspond to slow
 172 flow regions).

173 To mitigate the impact of substantial differences in observed surface velocity
 174 magnitude across various areas, we also define "relative overheating" (ROH) and
 175 "relative overcooling" (ROC), dividing AOH and AOC by the observed surface velocity
 176 magnitude respectively:

$$177 \quad ROH = \frac{\max(0, U_{sm} - U_{obs})}{U_{obs}}, \quad (3)$$

$$178 \quad ROC = (T_{melt} - T_{bm}) \times \frac{U_{bm}}{U_{obs}}. \quad (4)$$

179

180 **2.1.2 Normalization and ranking**

181 Overheating and overcooling inconsistencies are calculated on thawed bed and
 182 frozen bed, respectively. To evaluate the inconsistencies for the whole domain, we
 183 linearly normalized the overheating inconsistency and overcooling inconsistency to
 184 range from 0 to 1 and then sum them as:

$$185 \quad ACI = L_N(AOC) + L_N(AOH), \quad (5)$$

$$186 \quad RCI = L_N(ROC) + L_N(ROH), \quad (6)$$

187 where ACI means absolute combined inconsistency, RCI represents relative combined
 188 inconsistency, and L_N represents linear normalization. Taking AOC as an example, its
 189 linear normalization is:

190
$$L_N(AOC) = \frac{AOC - AOC_{min}}{AOC_{max} - AOC_{min}}. \quad (7)$$

191 Therefore, we obtain three absolute inconsistencies (AOH, AOC, ACI) and three
192 relative inconsistencies (ROH, ROC, RCI), with which we can comprehensively
193 analyze the temperature-sliding inconsistency in the inversion results of ice sheet model.
194 For each metric, we rank the eight GHF datasets from ~~1~~one (least inconsistent) to ~~8~~eight
195 (most inconsistent). The final score for each dataset is the average of its ranks across
196 the six metrics to ensure a comprehensive evaluation, as a reasonable simulation result
197 should perform well across thawed bed, frozen bed, and the whole region. We only
198 consider grounded ice and exclude points located at the domain boundary due to
199 relatively poor model performance there.

200 The specific metrics that we use to quantify this inconsistency could be adaptable,
201 for example by using a squared error term instead of the linear error terms that we used.
202 However, the general practice of emphasizing and quantifying the inconsistency
203 between a sliding inversion and the temperature/rheology field used as an input to that
204 inversion is novel.

205

206 **2.23 Methodology in Huang et al. (2024)**

207 In this study, we validate our method by comparing our ranking of GHF datasets
208 to the observationally constrained ranking established by Huang et al. (2024). For
209 readers not familiar with this paper, we provide here a brief summary of their method
210 and, in the next section, clarify the distinction between their paper and the present study.

211 Huang et al. (2024) employed thermo-mechanical coupled simulations using eight
212 GHF datasets to investigate the steady-state thermal regime of Totten Glacier. The
213 methodology comprised two interconnected modeling components:

- 214 1. Forward Modeling: An enhanced shallow-ice approximation model integrated with
215 a subglacial hydrology module was utilized to simulate englacial temperature profiles.
- 216 2. Inverse Problem: A full-Stokes ice flow model was applied to resolve the basal
217 friction coefficients through inverse analysis, to minimize the misfit between simulated
218 and observed velocities while simultaneously generating velocity predictions.

219 A feedback loop was then established: the velocity outputs from the inverse model
220 were used to refine key parameters in the forward model - specifically constraining the
221 basal slip ratio, rheological properties, and shape functions. This bidirectional coupling
222 process underwent multiple iterations to achieve convergent steady-state solutions.

223 Huang et al. (2024) utilized radar specular content data to differentiate localized
224 wet (thawed) versus dry (frozen) basal conditions and used this data as a two-sided
225 constraint on the basal thermal state. They compared modeled basal thermal states
226 derived from different GHFs to evaluate the reliability of the GHF datasets.

227

2.3.4 Distinction from Huang et al. (2024)

In Huang et al. (2024), modelled surface velocity velocities are compared with observations over the whole domain during the inversion for basal parameters for each GHF dataset. Here, surface velocities act as the observational constraints for the mechanical inversion.

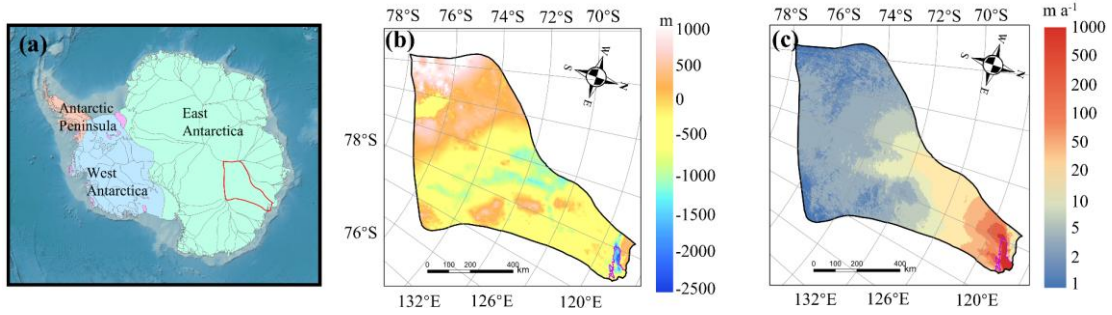
Although the overheating metrics here use the surface velocities and can thus be considered a subset of the inversion residual, our overcooling metrics are based on the basal sliding velocity derived from the inversion, which is not part of the mechanical inversion's residual. A mechanical inversion does not take into account the physical plausibility of the sliding result it produces. Therefore, it is not circular reasoning to compare two different parts of a model to each other; rather, it is an assessment of internal consistency, or lack thereof. A mechanical inversion may fit the surface velocity observations equally well when forced with many different models of the ice sheet thermal structure and rheology; however, if some models require high sliding velocities in frozen-based regions, then they should be downweighted in comparison to models that show a good agreement between basal temperature and velocity.

The method here does not require any additional observations beyond the surface velocities used in the mechanical inversion. However, there are “independent constraints” in the method here, which are not observations, but rather the a priori physical understandings that: 1) rapid sliding requires warm basal temperatures and subglacial water; 2) reducing the basal slip coefficient cannot prevent the ice from flowing by internal shear deformation. The inconsistency metrics developed in this paper are an attempt to quantify and rank the extent to which these basic (and uncontroversial) physical understandings are violated.

3. Application to Totten Glacier with Different GHFs

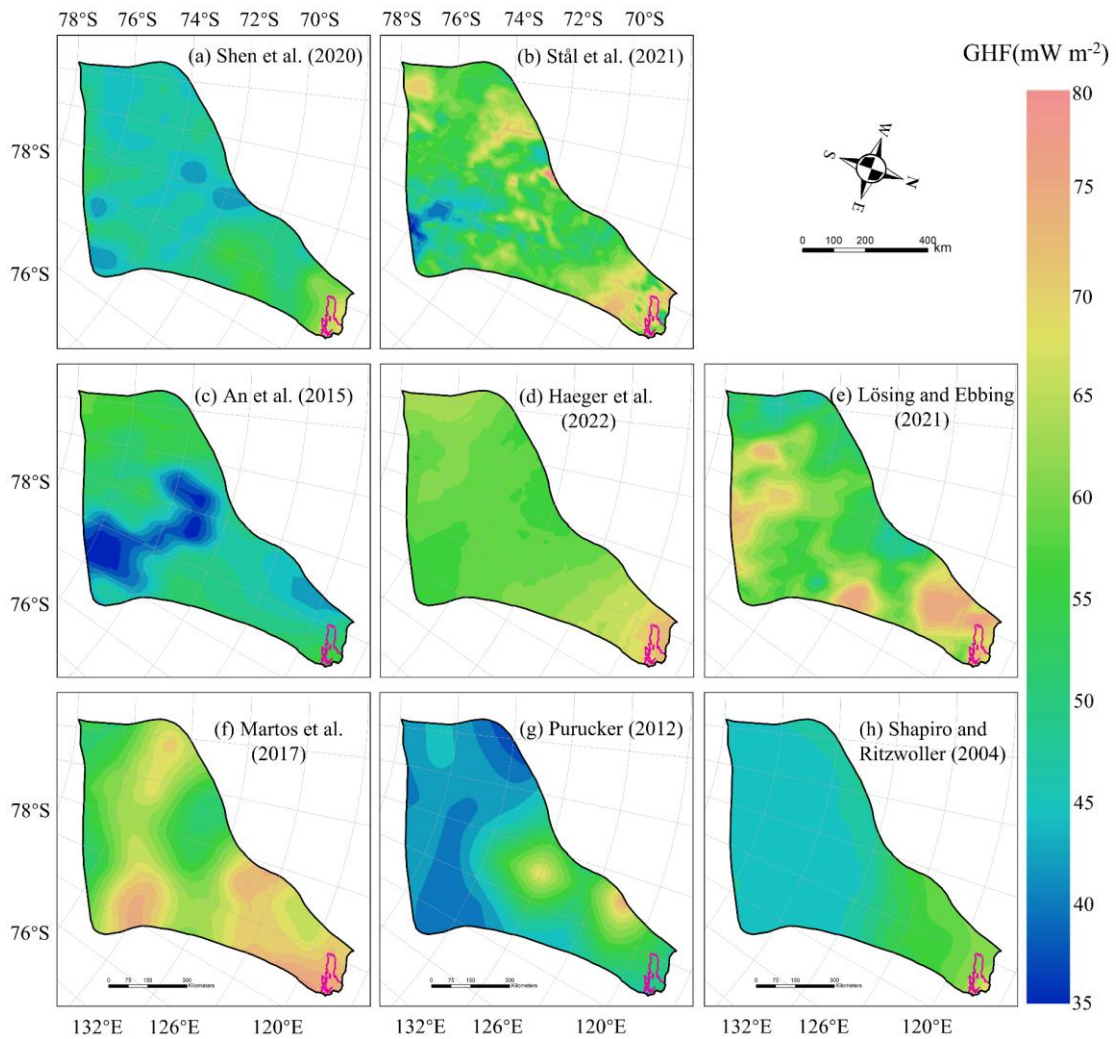
3.1 Study domain and Data

We apply our method to evaluate simulated ice temperature and ice velocity in Totten Glacier with eight GHF datasets by Huang et al. (2024). Huang et al. (2024) used the present-day surface ice temperature (Le Brocq et al., 2010), observed surface velocity from MEaSURES InSAR-Based Antarctic Ice Velocity Map, version 2 (Rignot et al., 2017) and ice sheet topography data from BedMachine Antarctica, version 2 (Morlighem et al., 2020). The eight GHF datasets were derived by various methodologies, resulting in significant differences in both spatial distribution and magnitude (Fig. 2). GHF fields from Stål et al. (2021), Haeger et al. (2022), Lösing and Ebbing (2021) and Martos et al. (2017) generally exhibit higher magnitudes than the other GHFs. Table S1 summarizes the input datasets, which follows the configuration described in Huang et al. (2024).



267
268
269
270
271

Figure 1. (a) Geographic location of Totten Glacier (red outline) in Antarctica; (b) bed elevation of Totten Glacier, the purple curve represents the grounding line; (c) observed surface velocity.



272
273
274

Figure 2. The spatial distribution of the eight GHF datasets for Totten Glacier (a–h) used as input data in Huang et al. (2024). The purple line depicts the grounding line.

275

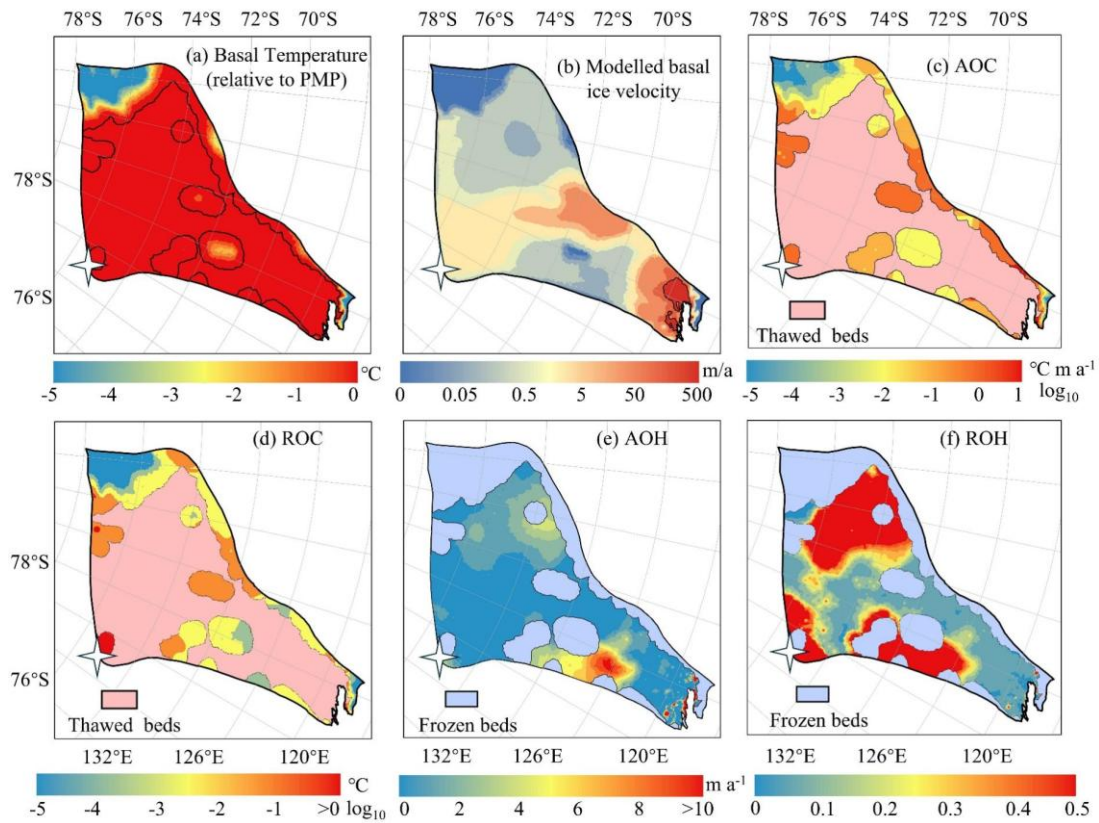
276 The spatial distribution of modelled basal temperature using the [eight](#) GHFs
277 displays both similarities and heterogeneity. In the northern part of Totten Glacier, there
278 is a consistent thawed-bedded pattern across all eight simulation results (Fig. S1), which
279 originates from the grounding line and extends upstream to approximately 71°S. This
280 thawed-bedded area is not contiguous with the lateral boundaries of Totten Glacier but
281 is instead bordered by frozen bed. All [eight](#) GHF datasets produce low basal ice
282 temperatures in the inland southwest, with Purucker et al. (2012), Shapiro and
283 Ritzwoller (2004), Shen et al. (2020) and Lösing and Ebbing (2021) being colder than
284 the other four GHF products. The basal ice velocities modelled from the [eight](#) different
285 GHF datasets produce similar spatial distributions (Fig. S2), which can be expected as
286 they were derived using the same inverse method and constrained by the identical
287 observed surface ice velocity. The modelled basal ice velocity is fast near the grounding
288 line and its upstream area. There are also high velocities between 70°S and 72°S close
289 to the western boundary of Totten Glacier (Fig. 1c), which are associated with
290 subglacial canyon features in the basal topography (Fig. 1b) and observed fast surface
291 ice velocity there.

292

293 **3.2 Spatial Distribution of Inconsistencies with one GHF dataset**

294 In this section, we show the spatial fields of the inconsistency metrics (Section 2.1
295 [and 2.2](#)) for the modelled result in Huang et al. (2024), using Martos et al. (2017) GHF
296 as an example. This example illustrates the interpretation process before conducting a
297 comprehensive comparative analysis for the result with [eight](#) GHF datasets.

298



299

300 **Figure 3.** Spatial distribution of modelled basal ice temperature (a), modelled basal ice
 301 velocity magnitude (b), AOC (c), ROC (d) inconsistencies in modelled frozen-bedded
 302 regions, and AOH (e) and ROH (f) inconsistencies in modelled thawed-bedded regions
 303 associated with Martos et al. (2017) GHF. The colormap in (c) and (d) is on logarithmic
 304 scale. The pink region in (c) and (d) represents modelled thawed bed, while the blue
 305 region in (e) and (f) indicates frozen-bedded areas. The white star represents Dome C.

306

307 The modelled result based on the Martos et al. (2017) GHF reveals extensive
 308 regions of thawed bed with limited areas of frozen bed. The frozen bed is predominantly
 309 located in the southern corner of the study domain, where the modelled basal velocity
 310 magnitude approaches zero, consistent with cold basal ice temperature. Consequently,
 311 the AOC inconsistency at this marginal zone is negligible (Fig. 3). Along the western
 312 margin of Totten Glacier, basal ice temperature remains below the pressure melting
 313 point, albeit approaching it. However, localized regions exhibit high basal velocities of
 314 several tens of meters per year, contradicting the presence of a frozen bed and resulting
 315 in large AOC inconsistencies.

316

317 Conversely, large AOH values are observed between 69°S and 71°S in the eastern
 318 Totten Glacier region, where the simulated surface velocity magnitude exceeds
 observational data by $>5 \text{ m a}^{-1}$ (Fig. 3e). In this area, the modelled basal ice temperature

319 reaches the pressure melting point, with the modelled basal velocity magnitude at
 320 approximately 0.05 m a^{-1} . Basal friction inversion failed to reproduce observed surface
 321 velocity magnitude due to the model's overestimation of ice temperature and softness.
 322 This pronounced velocity mismatch highlights a fundamental inconsistency in the
 323 eastern glacier region, likely originating from discrepancies in the input datasets.
 324 Regions of high ROH and ROC values coincide with areas of relatively high AOH and
 325 AOC, particularly where the observed surface velocities are slow, as per their
 326 formulations.

327

328 **3.3 Spatial Distribution of Inconsistencies with eight GHF datasets**

329

330 **3.3.1 Overcooling Inconsistency on Frozen Beds**

331 We calculated the inconsistency metrics for the thawed and frozen beds
 332 respectively, and summed the values over the corresponding regions. The results are
 333 shown in Table 1. To visualize the spatial heterogeneity of these inconsistencies, we
 334 mapped the distribution of the metrics. The spatial distribution of AOC reveals that
 335 most GHF datasets exhibit significant local overcooling inconsistencies at the
 336 subglacial canyon between 70°S and 72°S (Fig. 4). There is fast basal sliding in the
 337 inverse model results (Fig. S2), however, the modelled basal ice temperatures inferred
 338 from most of the GHF datasets are below the pressure melting point (Fig. S1). High
 339 specular content in radar data (Fig. 4c) suggests the presence of basal water in the
 340 subglacial canyons here (Dow et al., 2020; Huang et al., 2024), which also suggests that
 341 the basal ice temperature should be at the pressure melting point and confirms the
 342 inconsistency between the modelled temperature and velocity fields.

343 The area near the grounding line is characterized by fast ice flow (Fig. S2) and
 344 thawed bed (Fig. 4), yet some of the margin is frozen-bedded with modelled basal
 345 temperature below the pressure melting point, resulting in high AOC. Overall, modelled
 346 results with most GHF datasets show small overcooling inconsistencies. The modelled
 347 results using GHF from Purucker et al. (2012), Shapiro and Ritzwoller (2004), Shen et
 348 al. (2020), Lösing and Ebbing (2021) exhibit no overcooling inconsistency in
 349 southwestern Totten Glacier (Fig. 4). The largest value of ROC across most GHF occurs
 350 at Dome C (white star in Figure 5), where the observed surface ice velocity magnitude
 351 is close to zero (Fig. 1c).

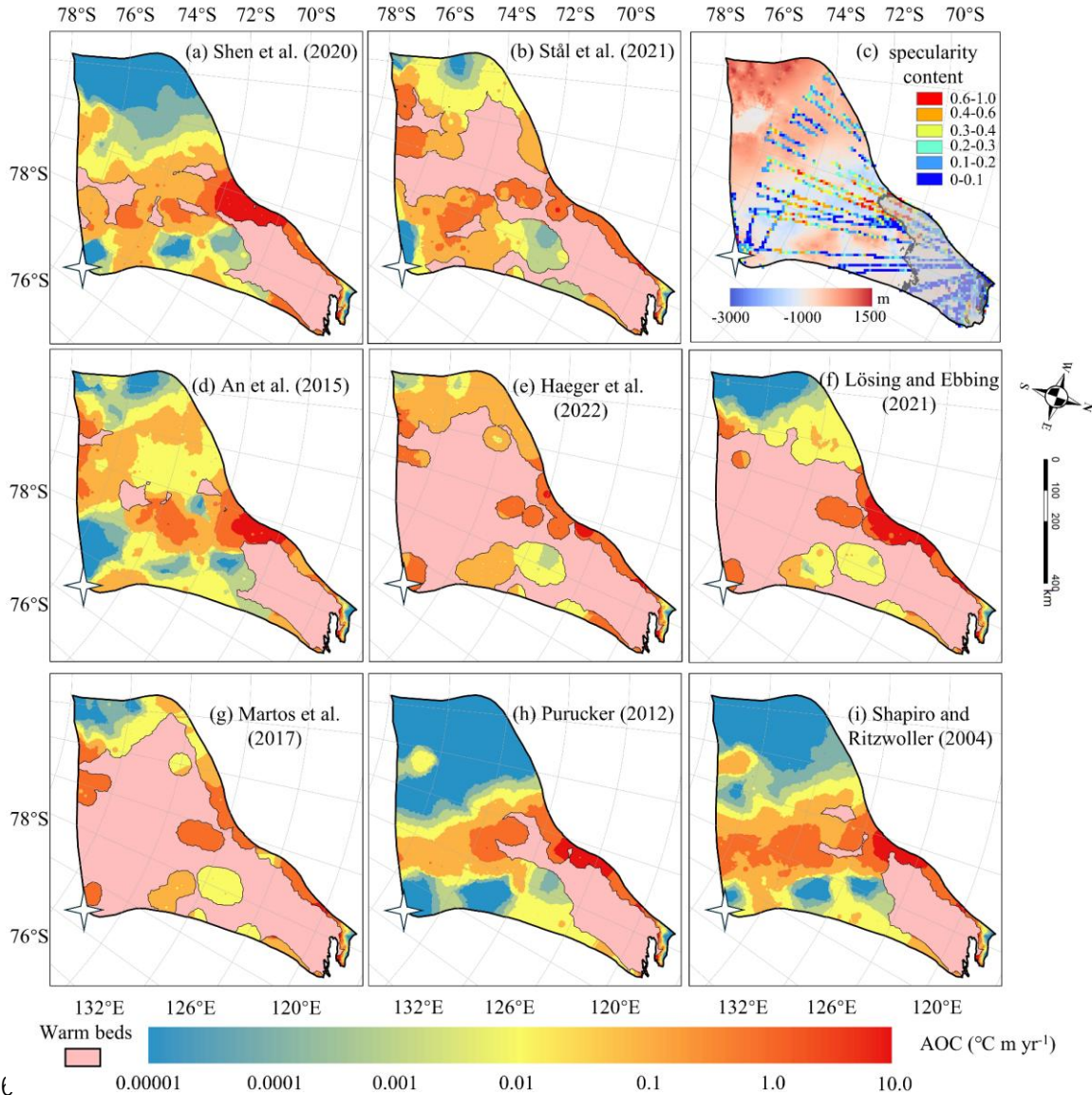
352

353 Table 1. Summary of inconsistency metrics for different GHF maps.

| GHF maps | AOC ($^{\circ}\text{C km yr}^{-1}$) | AOH (km yr^{-1}) | ROC ($^{\circ}\text{C}$) | ROH | ACI | RCI |
|--------------------|--|--------------------------------|-------------------------------|-----|------|------|
| Shen et al. (2020) | 6.39 | 29 | 159 | 470 | 0.59 | 0.39 |
| Stål et al. (2021) | 6 | 31.9 | 144 | 814 | 0.84 | 0.8 |

| | | | | | | |
|-------------------------------|------|------|-----|------|------|------|
| An et al. (2015) | 5.97 | 30.5 | 130 | 397 | 0.53 | 0.11 |
| Haeger et al. (2022) | 6.32 | 34.1 | 126 | 889 | 1.51 | 1.57 |
| Lösing and Ebbing (2021) | 6.91 | 34.1 | 290 | 780 | 1.97 | 1.58 |
| Martos et al. (2017) | 5.82 | 34.2 | 146 | 1072 | 1.14 | 1.18 |
| Purucker (2012) | 5.89 | 30.6 | 115 | 375 | 0.5 | 0 |
| Shapiro and Ritzwoller (2004) | 5.65 | 31.8 | 138 | 417 | 0.54 | 0.19 |

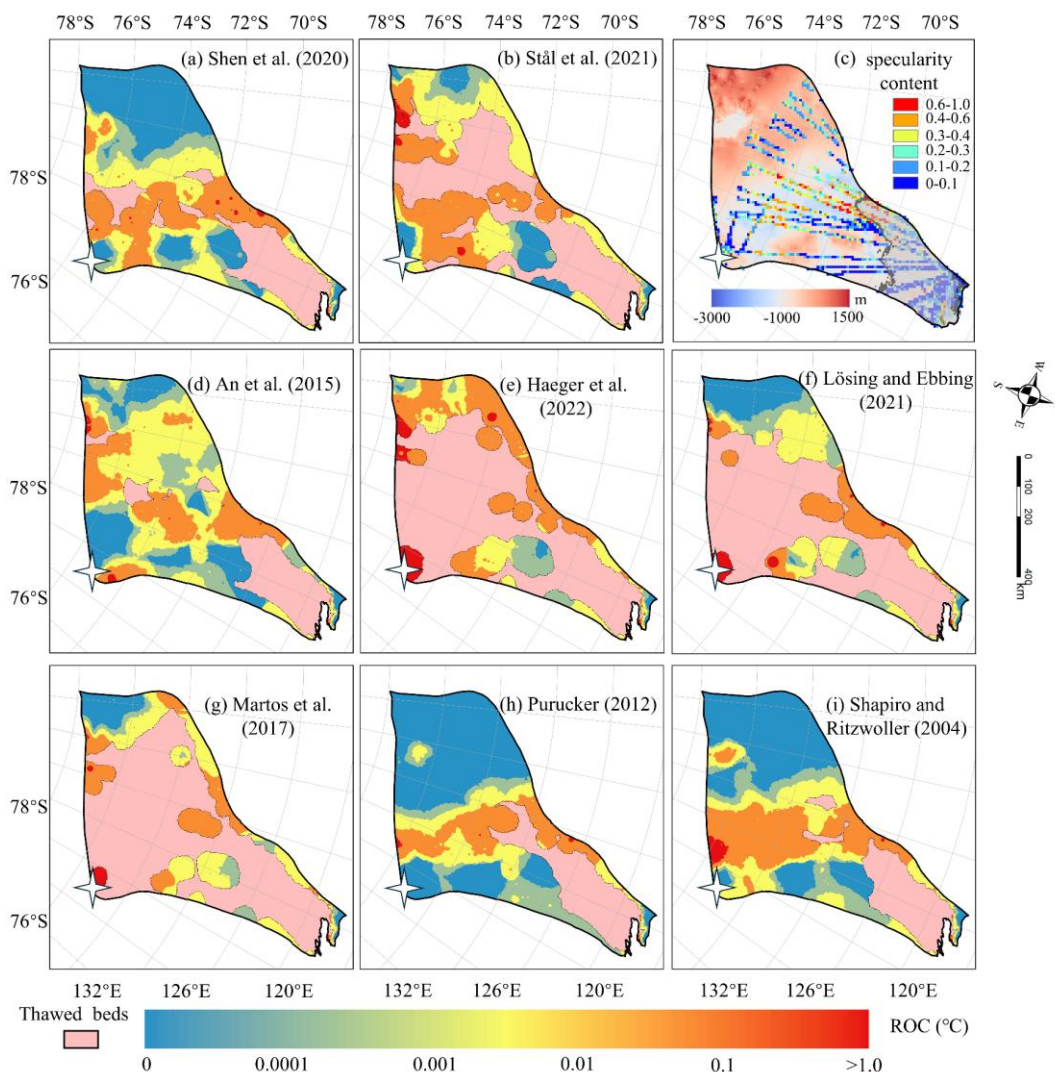
354
355



356
357
358
359

Figure 4. Spatial distribution of AOC inconsistency in modelled frozen-bedded regions (a-b, d-i) associated with the GHFs (a-h) in Fig. 2. The colormap is on logarithmic scale. The pink region represents modelled thawed bed. (c) Specularity content sourced

360 from radar data collected by ICECAP (Dow et al., 2020) with the bed elevation in the
 361 background. Gray area in (c) corresponds to surface velocity magnitude exceeding 30
 362 m yr⁻¹. The white star represents Dome C. Note the colormap is logarithmic.
 363



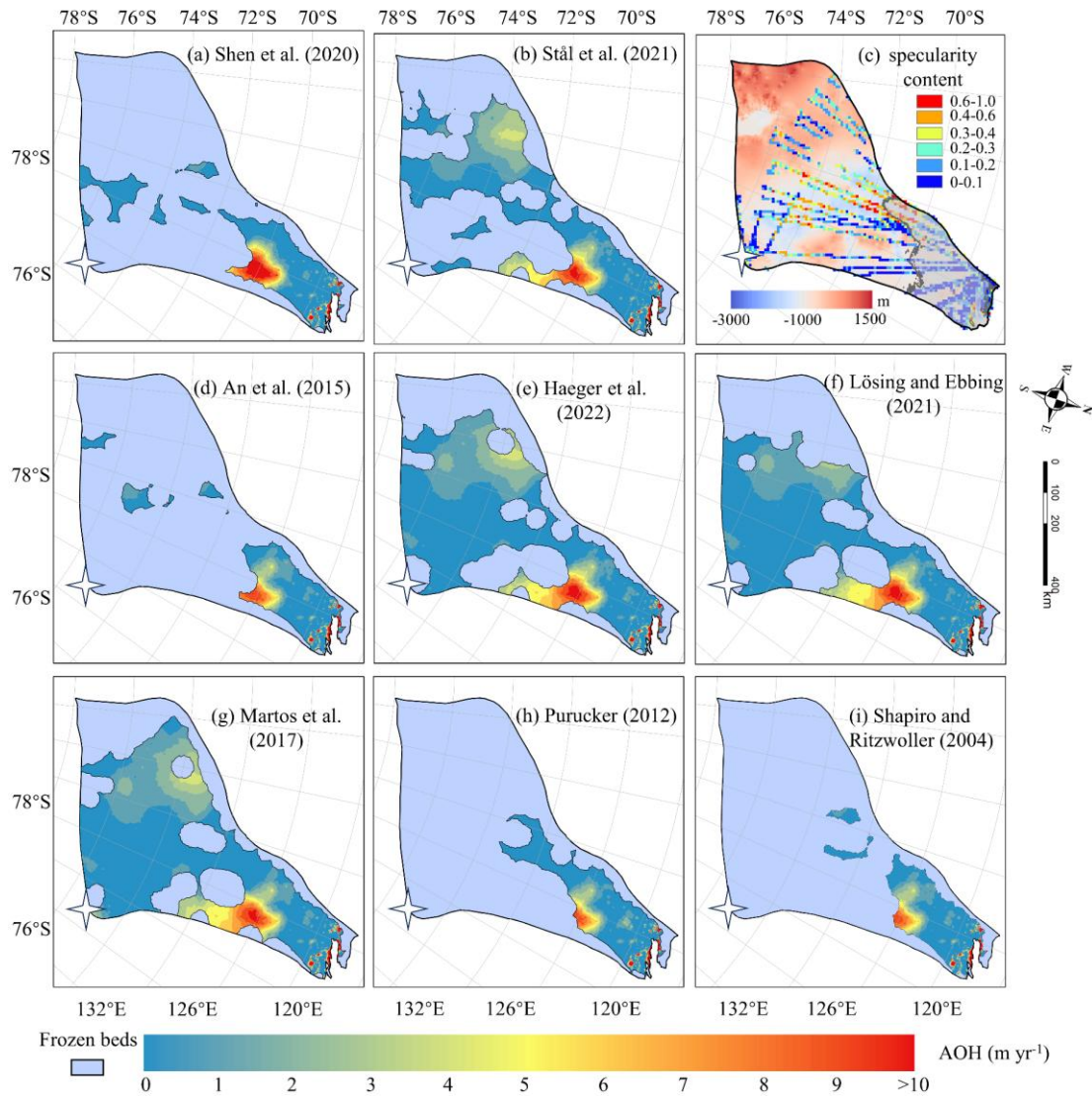
364
 365 **Figure 5.** The spatial distribution of relative overcooling (ROC) inconsistency in cool
 366 beds with (a), (b) and (d) to (i) corresponding to the GHFs (a - h) in Figure 2. The pink
 367 area represents the thawed beds. Dome C is marked by a white star. (c) Locations of
 368 specularity content derived from radar data collected by ICECAP (Dow et al., 2020)
 369 and with the bed elevation in the background. The gray curve is the contour of the
 370 surface velocity magnitude of 30 m yr⁻¹. Note the colormap is logarithmic.
 371

371

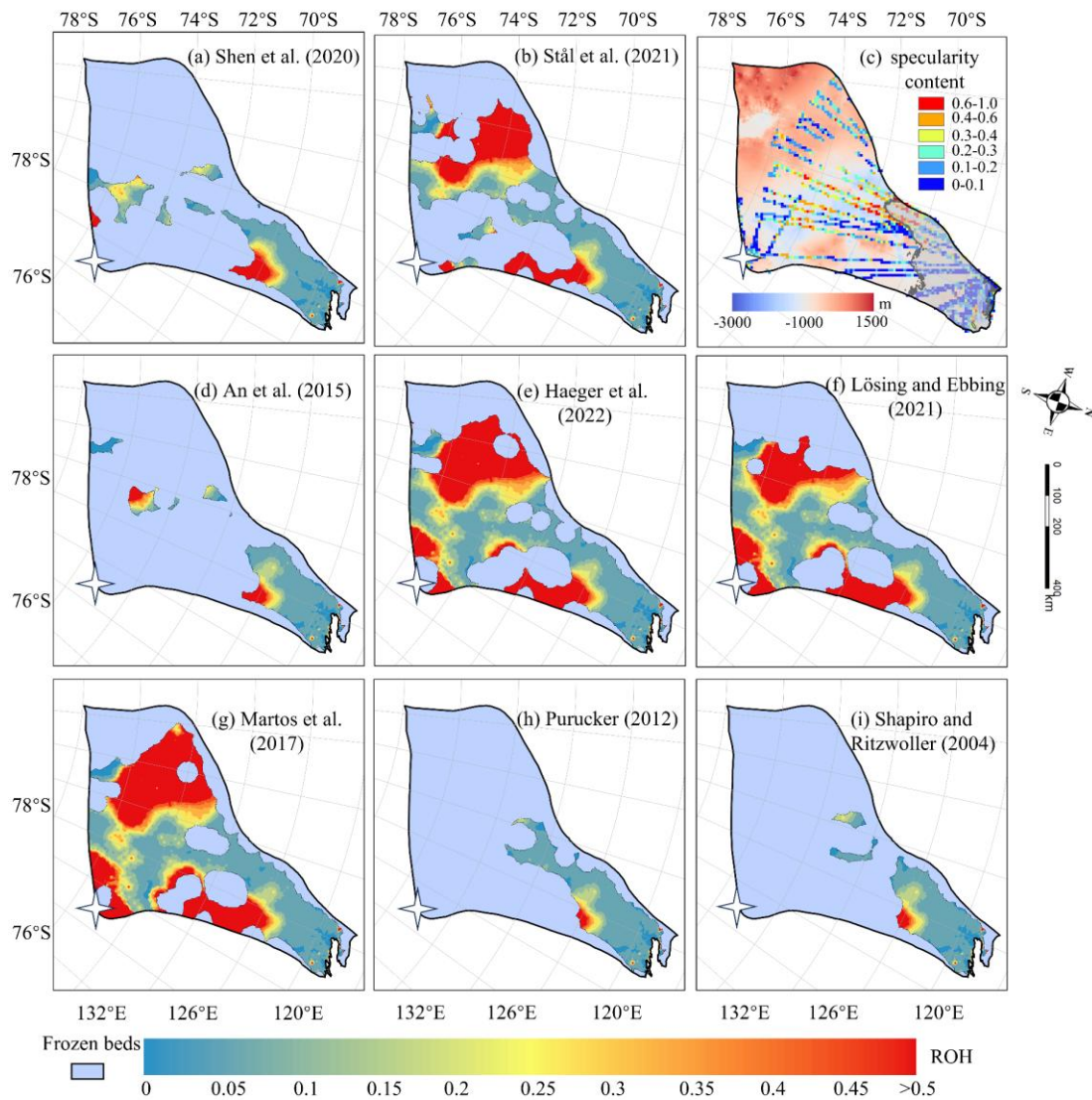
372 3.3.2 Overheating Inconsistency on Thawed Beds

373 The simulations with all eight GHFs yield similar spatial distributions of AOH

374 (Fig. 6) on the common area of thawed bed, and similar locations of high AOH values.
 375 A common high AOH area is located between 69°S and 72°S in the eastern part of
 376 Totten Glacier, due to simulated surface ice velocities greatly exceeding the observed
 377 surface ice velocities. Low specularity content from radar data (Fig. 6c) suggests there
 378 is no basal water in the area (Dow et al., 2020; Huang et al., 2024). Therefore, it is likely
 379 that the basal ice temperature is overestimated there. The simulations with all the eight
 380 GHFs also yield similar spatial distribution of ROH (Fig. 7), but its largest values are
 381 mostly in the slow flowing region as one may expect from its formulation (Eq. (3)).



382
 383 **Figure 6.** Spatial distribution of AOH in thawed-bedded regions with (a-b, d-i)
 384 corresponding to the GHFs (a-h) in Fig. 2. The blue region indicates frozen-bedded
 385 areas. (c) Locations of specularity content, same as Fig. 4c. The white star represents
 386 Dome C.



388

389 **Figure 7.** The spatial distribution of relative overheating (ROH) inconsistency in
 390 thawed beds with (a), (b) and (d) to (i) corresponding to the GHFs (a - h) in Figure 2.
 391 The light purple mask represents the frozen beds. (c) Locations of specularity content
 392 (coloured points), same as Fig. 6. The white star represents Dome C.

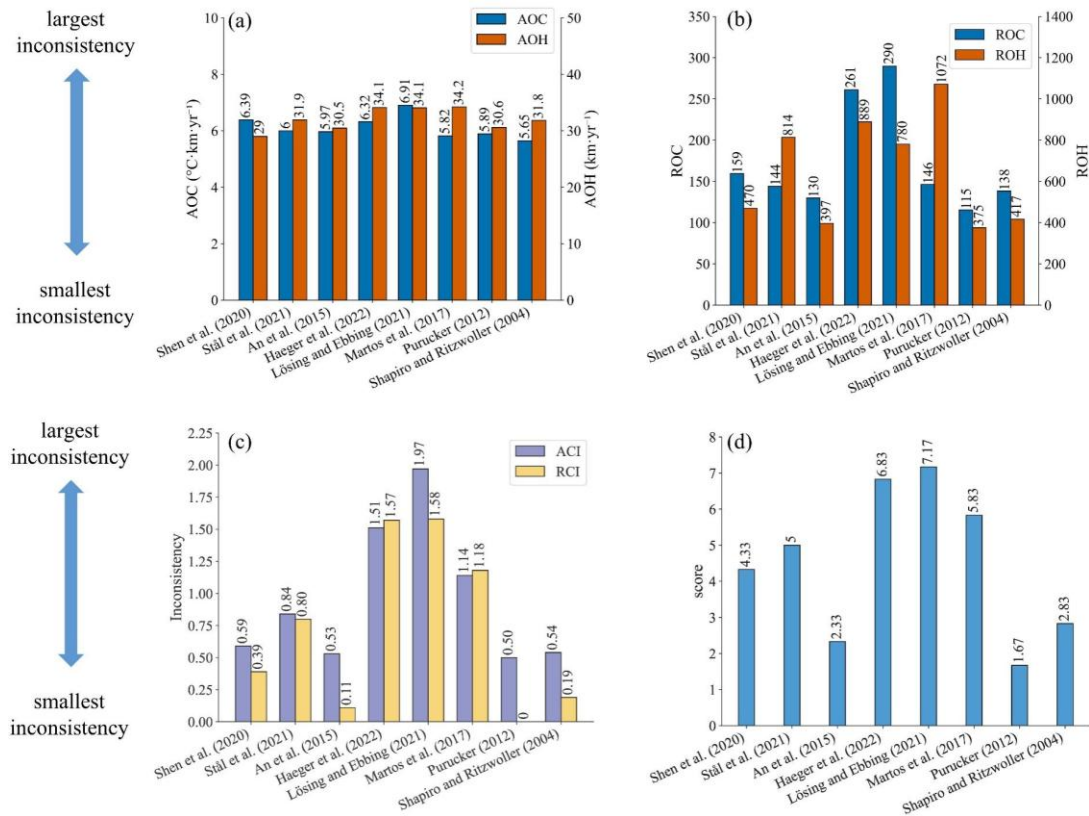
393

394 3.4 Evaluation of Model Inconsistency with Eight GHFs

395 To assess the overall inconsistency of each geothermal heat flux dataset, we
 396 calculate the sum of each metric over all points. All inconsistency indices for the
 397 simulation results using the eight GHF datasets are illustrated in Fig. 8. The overheating
 398 inconsistency associated with Purucker et al. (2012) and Shapiro and Ritzwoller (2004)
 399 GHFs is predominantly localized in fast-flowing regions. Consequently, after

400 normalization by the observed surface velocity magnitude, their relative rankings
401 improve (Fig. 8). The GHFs from Purucker et al. (2012), An et al. (2015), Shapiro and
402 Ritzwoller (2004), and Shen et al. (2020) demonstrate balanced performance with
403 respect to both overheating and overcooling inconsistency metrics, thereby securing the
404 top four positions in both ACI and RCI. Their ACI values exhibit similarity, ranging
405 from 0.50 to 0.59 (Fig. 8c). In contrast, simulation result utilizing Martos et al. (2017)
406 GHF exhibits low AOC but high AOH. Simulation results utilizing Stål et al. (2021)
407 GHF show low ROC but relatively high ROH. Notably, simulation results employing
408 GHFs from Martos et al. (2017), Haeger et al. (2022), and Lösing and Ebbing (2021)
409 demonstrate comparably high AOH values. These four GHF datasets—Martos et al.
410 (2017), Stål et al. (2021), Haeger et al. (2022), and Lösing and Ebbing (2021)—are
411 ranked in the bottom four positions for both ACI and RCI metrics. Furthermore, the
412 ranking order of the eight GHFs remains consistent between ACI and RCI.

413 The final averaged ranking (Fig. 8d) across the indices is also the same as that of
414 ACI and RCI. Purucker et al. (2012), An et al. (2015) and Shapiro and Ritzwoller (2004)
415 GHFs occupy the top three positions. Following closely, Shen et al. (2020) and Stål et
416 al. (2021) GHFs secure the 4th and 5th positions, respectively. Martos et al. (2017),
417 Haeger et al. (2022) and Lösing and Ebbing (2021) GHFs are ranked as the bottom
418 three among the eight GHFs in Totten Glacier. The thermal state produced by the
419 optimal GHF result shows that thawed beds predominantly cluster around the
420 grounding line and its upstream regions. Conversely, the inland areas of Totten largely
421 exhibit cold temperatures, with relatively sparse thawed-bedded areas.



422

423 **Figure 8.** Six inconsistency indicators and the final ranking of eight GHF datasets. **(a)**
 424 the absolute overcooling and overheating inconsistencies, AOC and AOH; **(b)**
 425 the relative overcooling and overheating inconsistencies, ROC and ROH; **(c)**
 426 the absolute and relative combined inconsistencies, ACI and RCI; **(d)**
 427 the average of ranking scores from one to eight using the six inconsistency indicators. The value
 428 values of inconsistencies and scores are labeled at the top of the bars.

429

430 4. Discussion

431 4.1 Sensitivity of Inconsistencies to GHF Datasets

432 Comparing the GHF dataset rankings between this study and Huang et al. (2024),
 433 we find that the top four and the bottom four are the same in the two studies, albeit
 434 with slight variations in ranking. The lower ranking of Shen et al. (2020) in this study
 435 may be attributed to several factors. Firstly, Huang et al. (2024) excludes areas with ice
 436 velocity magnitude exceeding 30 m a^{-1} (Fig. 4c) because specular content is an
 437 ambiguous indicator of wet beds there. Secondly, the GHF from Shen et al. (2020)
 438 yields higher basal temperature and also faster basal ice velocities in most of the frozen
 439 bed of Totten Glacier, hence exhibits greater overcooling inconsistency, compared with
 440 Purucker et al. (2012), leading to a decrease in its rankings (Fig. S3). Lastly, Huang et
 441 al. (2024) primarily relied on specular content, while our study evaluated datasets

442 based on inconsistencies in the simulation results. Despite these methodological
443 differences, both studies identified four relatively well-performing GHF datasets for
444 Totten Glacier, which exhibit similar distributions of thawed and frozen beds when
445 compared to the other four datasets (Fig. 4 and Fig. 6). This similarity underscores that
446 the thawed bed is concentrated near and upstream of the grounding line. Datasets from
447 Stål et al. (2021), Martos et al. (2017), Haeger et al. (2022), and Lösing and Ebbing
448 (2021) exhibit a tendency to overestimate GHF in central Totten Glacier.

449 Simulations employing GHF datasets from Stål et al. (2021), Martos et al. (2017),
450 Haeger et al. (2022), and Lösing and Ebbing (2021) yield more extensive thawed-
451 bedded regions and are expected to exhibit greater overheating inconsistency.
452 Nevertheless, these models also exhibit relatively high overcooling inconsistency
453 despite the limited extent of frozen-bedded regions. We quantified the discrepancies
454 between these four GHF datasets and the Purucker et al. (2012) GHF in terms of
455 modelled basal velocity, basal temperature relative to the pressure melting point, and
456 AOC (Fig. S4). The Purucker et al. (2012) GHF yields lower basal ice temperatures and
457 slower basal velocities across most frozen-bedded regions, consequently resulting in
458 lower AOC values compared to the other four GHF datasets.

459

460 **4.2 Causes of Inconsistencies and Sources of Uncertainty**

461 We have developed an indirect method that utilizes surface velocity observations
462 to assess the quality of simulated basal temperature. However, the mere fact that
463 inconsistencies exist does not by itself tell us what caused those inconsistencies.
464 Broadly speaking, the measured inconsistencies can come from two sources:
465 temperature or velocity. Uncertainties in any of the input datasets used to compute those
466 two fields can produce inconsistencies, as can simplifications in the model physics.
467 Here, we have tested the influence of one particular boundary condition, GHF, since
468 that field is particularly hard to constrain. Because all other inputs are kept constant,
469 the differences in the inconsistencies that we calculated between different simulations
470 can be attributed to the GHF fields. However, we also found that all of the models we
471 tested had non-zero inconsistency (Fig. 4; Fig. 6). The absolute inconsistencies, AOH
472 and AOC, had particularly small between-model variability in comparison to their mean
473 value. This could be related to uncertainties or limitations in the input GHF fields, but
474 it may also indicate sensitivities to other model inputs. For instance, the surface
475 temperature used in Huang et al. (2024) represents the present-day climate, but the
476 thermal structure of the ice sheet may reflect colder temperatures during the last glacial
477 cycle. We discuss an additional experiment we performed to test the influence of
478 uncertainty in surface temperature on our inconsistency metrics in Section 4.3 below.
479 While the cooler surface temperatures during the glacial period exerted a cooling effect
480 on ice sheet temperature, lower surface accumulation rates over the same period

481 induced a warming effect. Uncertainties in bed topography should influence both our
482 thermal and our mechanical models, with deeper ice being more likely to be warm, and
483 with errors in ice thickness producing compensating errors in basal sliding in our
484 mechanical inversion. In the study of Huang et al. (2024), BedMachine v2 was used for
485 ice thickness and subglacial topography. However, Bedmap3 (Pritchard et al., 2025)
486 has better-resolved mountains and smoother trough margins.

487 The simulation results we use from Huang et al. (2024) came from a 3D isotropic
488 full-Stokes ice flow model. While full-Stokes is generally considered an ice sheet model
489 with the most complete physical processes to date, the use of an isotropic rheology may
490 not be valid in some parts of the ice sheet, such as near ice divides or at the margin of
491 an ice stream where the history of past ice deformation creates anisotropic crystal fabric
492 that affects the present-day mechanical properties (Martín et al., 2009; Zhao et al., 2018;
493 Zwinger et al., 2014). Isotropic flow laws often require the use of an “enhancement
494 factor” for vertical shear in the lower part of the ice column, an ad hoc correction that
495 would have a particularly large influence on our computed overcooling metrics. Thus
496 the isotropic flow law potentially introduces errors in modelled strain rates and, hence,
497 bias in basal sliding velocities obtained by inversion methods (Budd and Jacka, 1989;
498 Gerber et al., 2023; Rathmann and Lilien, 2022). Simulated surface ice velocities can
499 be influenced by other factors in addition to ice fabric; shear margins are also impacted
500 by accumulated rupture, such as damage along a shear margin (e.g., Benn et al., 2022;
501 Lhermitte et al., 2020; Schoof, 2004; Sun et al., 2017). Ice deposited during the last
502 glaciation has different chemistry (especially concentrations of chloride and possibly
503 sulphate ions) which leads to smaller crystals that develop a strong, near-vertical,
504 single-maximum fabric (Paterson, 1991). However, ice fabric data is sparse, known
505 from direct observations at ice cores (Azuma and Higashi, 1985) or inferred from
506 specialized radar measurements (Fujita and Mae, 1994; Jordan et al., 2022), and its
507 impact is beyond the scope of this study as we refrain from incorporating additional
508 observational data relying only on widely-available surface ice velocities.

509 Our inconsistency metrics are designed to provide bidirectional constraints,
510 wherein the model is penalized for both overheating and overcooling. By adopting this
511 bidirectional constraint framework, we aim to mitigate the risk of unidirectional
512 constraints leading to excessively cold or warm outcomes being deemed optimal.
513 However, our inconsistency metrics only provide a bidirectional constraint when
514 viewed in a spatially integrated sense. Locally, we only have unidirectional constraints.
515 This is because our overheating metrics are only computed where the bed is at the
516 melting point, and our overcooling metrics are only computed where the bed is below
517 the melting point. This makes methodological sense, as sliding is generally expected to
518 occur where the bed is thawed. However, in reality it is entirely possible that some of
519 the areas where the modelled bed reaches the pressure melting point are still too cold

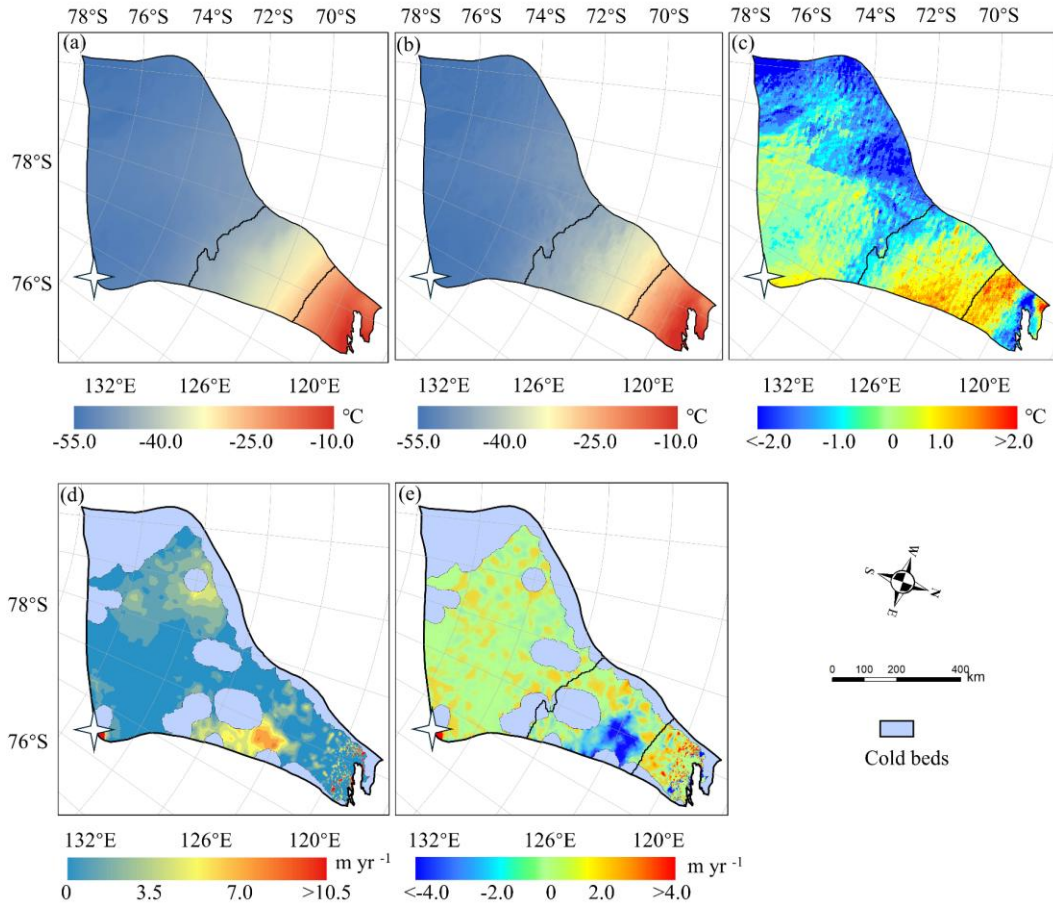
520 (the modelled melt rate is lower than the real melt rate), and conversely, it is also
521 possible that some of the areas where the modelled bed is below the pressure melting
522 point are still too warm (the real temperature is colder still). Our method cannot identify
523 these areas. Thus, our inconsistency metrics may underestimate variability in the ice
524 sheet thermal state: we have no way to penalize frozen regions that are not cold enough
525 or thawed regions that are not warm enough. We leave the development of these
526 constraints to future work.

527

528 **4.3 Impact of Input Datasets**

529 There is a common area between 69°S and 72°S in the eastern part of Totten
530 Glacier with the largest AOH (Fig. 6) for all the GHFs varying from 48 to 70 mW m⁻²,
531 which suggests that the AOH inconsistency is from other ice sheet properties rather than
532 GHF. Zhang et al. (2022) reconstructed Antarctic near-surface air temperature based on
533 MODIS land surface temperature measurements and in situ air temperature records
534 from meteorological stations from 2001 to 2018. We compared the reconstruction of
535 near-surface air temperature in the year 2001 (Zhang et al., 2022) and the ALBMAP v1
536 dataset used in Huang et al. (2024). The surface air temperature in the area with large
537 AOH from ALBMAP v1 is 0.6-3.1 °C higher than that from the reconstructed near-
538 surface air temperature in 2001 (Fig. 9). The MODIS-based near-surface air
539 temperature product shows warming in Totten Glacier from 2001 to 2018. Even so, the
540 surface air temperature in the area with large AOH from ALBMAP v1 is still higher
541 than that in 2018 but over a smaller area. Therefore, we infer that the large AOH may
542 be attributed to a warm bias in the present-day ice surface temperature derived from
543 ALBMAP v1 in this area. The englacial temperature will be lower than present-day ice
544 sheet surface temperature used in the model but warmer than the average surface
545 temperature during the last glacial-interglacial cycle. We lowered the surface ice
546 temperature in this area by 1 °C, reran the simulation, and found that AOH with all the
547 GHFs was halved (Fig. 9e).

548



549
 550 **Figure 9.** Surface ice temperature from ALBMAP v1 (a) and MODIS-based near-
 551 surface air temperature (b) in the year 2001, and their difference (c). (d) The AOH using
 552 modified surface ice temperature by reducing the temperature between the two black
 553 lines (contour lines of ≈ -44 °C and ≈ -26 °C) in (a) by 1 °C and GHF of Martos et al.
 554 (2017). (e) The difference between the AOH using cooler surface ice temperature and
 555 the original AOH. The white star represents Dome C.

556

557 4.4 Implications for Ice Sheet Dynamics

558 While evaluating inconsistencies highlights the spatial distribution of mismatches,
 559 it does not inherently elucidate their underlying causes. The primary factors to
 560 investigate are surface temperature, GHF, accumulation rate, and ice thickness,
 561 representing the most critical boundary conditions. Furthermore, integrating multiple
 562 sources of prior knowledge can help constrain model parameters:

- 563 1. High-resolution radar measurements: The availability of ice thickness data along
 564 flight lines should be assessed to validate geometric boundary conditions.
- 565 2. Paleoclimate context: Historical climate reconstructions indicate significantly colder
 566 surface temperatures during glacial periods compared to present-day conditions, with

567 correspondingly lower accumulation rates. These paleo-temperature conditions likely
568 induced a long-term thermal memory within the ice column, potentially contributing to
569 observed discrepancies between modeled and measured basal properties.

570 Therefore, we recommend a systematic evaluation of: (1) The spatial distribution
571 of radar-derived ice thickness measurements; (2) The temporal consistency of surface
572 temperature boundary conditions; (3) The sensitivity of model results to GHF variations;
573 (4) Accumulation rate reconstructions during key climatic periods. This multi-faceted
574 approach helps isolate the causes of inconsistencies in ice sheet simulations.

575 Given that data assimilation and inverse methods are widely employed to infer
576 basal friction coefficients in ice sheet simulations, it is essential to acknowledge the
577 impact of the inconsistencies identified in our study on ice sheet dynamics. A frozen
578 bed is supposed to provide substantial resistance and limit basal sliding; however, if the
579 basal temperature is overestimated, it may decrease viscosity and enhance basal sliding.
580 This overheating inconsistency would lead to an overestimation of ice flow speeds,
581 discharge, and dynamic ice loss (Artemieva, 2022; Burton-Johnson et al., 2020).
582 Similarly, underrepresentation of thawed bed conditions will lead to an underestimation
583 of ice discharge and, consequently, an underestimation of ice sheet's response to climate
584 warming. The basal thermal regime critically influences the stability of grounding lines
585 and the behavior of ice streams (Dawson et al., 2022; Robel et al., 2014). In a warming
586 climate, increases in geothermal or frictional heating can trigger basal thawing in these
587 areas, lowering basal friction and potentially initiating rapid grounding line retreat—a
588 key component of marine ice sheet instability (MISI) (Reese et al., 2023; Ross et al.,
589 2012). Without incorporating a self-consistent thermal model into the inversion,
590 projections may misrepresent the onset and extent of these dynamic instabilities. Our
591 findings underscore that a fully coupled inversion framework would use not only
592 surface velocity data but also incorporate direct or proxy observations of basal
593 temperature and subglacial hydrology. Such an approach would better constrain the
594 basal friction coefficient in a physically consistent manner, reducing the risk of
595 producing nonphysical states. This integration is especially critical for projections of
596 ice sheet evolution under future climate change scenarios, as the dynamic response is
597 sensitive to even small changes in basal conditions.

598

599 **5. Conclusion**

600 We propose a novel and rapid method to quantify the inconsistencies between
601 modelled basal ice temperature and observed surface velocity magnitude and assess the
602 quality of ice sheet model simulation results without using subglacial observation data.

603 ~~Previously, it has been assumed that assessing the quality of an ice sheet temperature~~
604 ~~model required in situ observations, whether from ice cores or geophysical techniques~~
605 ~~like ice penetrating radar.~~ By using the ice temperature field to compute the rheology

606 structure needed for a mechanical inversion and then quantifying the inconsistency
607 between the inverted velocity field and the original ice temperature field, we are able
608 to use remotely sensed surface velocity observations as a means to assess on the quality
609 of modelled basal temperatures. Given the challenges in acquiring subglacial data, our
610 method can provide a streamlined and effective approach to evaluation.

611 We apply this method to evaluate the steady-state simulation results of Totten
612 Glacier presented by Huang et al. (2024), which were derived using a 3D full-Stokes
613 model with eight different GHF datasets. Assuming the inconsistencies are mainly due
614 to quality issues of GHF datasets, we use the inconsistencies to assess the reliability of
615 those GHF datasets. We compare our GHF ranking with that by Huang et al. (2024)
616 which used specularly content to derive a two-sided constraint on the basal thermal
617 state. We find that the top four and the bottom four GHFs are the same in the two
618 studies, albeit with slight variations in ranking. Furthermore, we find that the
619 simulations with all GHF datasets underestimate the basal ice temperature in a canyon
620 on the western boundary of Totten Glacier, and we infer that the common high
621 overheating inconsistencies with all the GHF datasets in the eastern Totten Glacier
622 between 69°S and 72°S may be attributed to a warm bias in the prescribed surface ice
623 temperature used in the model. While we demonstrate that this approach works on
624 simulation results for Totten Glacier, testing of the method on other glaciers would be
625 useful to assess if the approach is worthwhile for revealing ambiguous conflicts in
626 observations and simulations.

627
628 *Data availability.* MEaSURES BedMachine Antarctica, version 2, is available at
629 <https://doi.org/10.5067/E1QL9HFQ7A8M> (Morlighem, 2020); last access: 4 January
630 2026). MEaSURES InSAR-Based Antarctic Ice Velocity Map, version 2, is available at
631 <https://doi.org/10.5067/D7GK8F5J8M8R> (Rignot et al., 2017; last access: 4 January
632 2026). MEaSURES Antarctic Boundaries for IPY 2007–2009 from Satellite Radar,
633 version 2, is available at <https://doi.org/10.5067/AXE4121732AD> (Mouginot et al.,
634 2017; last access: 4 January 2026). ALBMAP v1 and the GHF dataset of Shapiro and
635 Ritzwoller (2004) are available at <https://doi.org/10.1594/PANGAEA.734145> (Le
636 Brocq et al., ~~2010~~-2010; last access: 4 January 2026). MODIS-based near-surface air
637 temperature data are available at <https://doi.org/10.11888/Atmos.tpdc.272234> (Zhang,
638 2022; last access: 4 January 2026). The GHF dataset of An et al. (2015) is available at
639 <http://www.seismolab.org/model/antarctica/lithosphere/AN1-HF.tar.gz> (last access: ~~11~~
640 ~~April 2023~~ 4 January 2026). The GHF dataset of Shen et al. (2020) is available at
641 <https://sites.google.com/view/weisen/research-products?authuser=0> (last access: ~~11~~
642 ~~April 2023~~ 4 January 2026). The GHF dataset of Martos (2017) is available at
643 <https://doi.org/10.1594/PANGAEA.882503>; (last access: 4 January 2026). The GHF
644 dataset of Purucker (2012) is available at

645 https://core2.gsfc.nasa.gov/research/purucker/heatflux_mf7_foxmaule05.txt (last
646 access: 11 April 2023). [The modelled basal temperature and basal melt rate from Huang
647 et al. \(2024\) are available at <https://doi.org/10.5281/zenodo.7825456> \(Zhao et al., 2023;
648 last access: 4 January 2026\).](#)

649

650 *Author contributions.* LZ and JCM conceived the study. LZ, MW, and JCM designed
651 the methodology. JW and LZ analyzed the data and conducted visualization. JW
652 and LZ wrote the original draft, and all the authors revised the paper.

653

654 *Competing interests.* The contact author has declared that none of the authors has any
655 competing interests.

656

657 *Acknowledgements.* This work was supported by National Natural Science Foundation
658 of China (grant no. 42576280) and Academy of Finland (grant no. 355572). [The
659 authors would like to thank the editor, Gong Cheng, and the anonymous reviewers
660 for their constructive comments and suggestions, which improved the quality and
661 clarity of this manuscript.](#)

662

663 **References**

- 664 Albrecht, T., Winkelmann, R., and Levermann, A.: Glacial-cycle simulations of the Antarctic Ice
665 Sheet with the Parallel Ice Sheet Model (PISM) – Part 1: Boundary conditions and climatic
666 forcing, *The Cryosphere*, 14, 599–632, <https://doi.org/10.5194/tc-14-599-2020>, 2020.
- 667 An, M., Wiens, D. A., Zhao, Y., Feng, M., Nyblade, A., Kanao, M., Li, Y., Maggi, A., and L ev eque,
668 J.: Temperature, lithosphere-asthenosphere boundary, and heat flux beneath the Antarctic Plate
669 inferred from seismic velocities, *J. Geophys. Res. Solid Earth*, 120, 8720–8742,
670 <https://doi.org/10.1002/2015JB011917>, 2015.
- 671 Artemieva, I. M.: Antarctica ice sheet basal melting enhanced by high mantle heat, *Earth-Sci. Rev.*,
672 226, 103954, <https://doi.org/10.1016/j.earscirev.2022.103954>, 2022.
- 673 Azuma, N. and Higashi, A.: Formation Processes of Ice Fabric Pattern in Ice Sheets, *Ann. Glaciol.*,
674 6, 130–134, <https://doi.org/10.3189/1985AoG6-1-130-134>, 1985.
- 675 Benn, D. I., Luckman, A.,  str om, J. A., Crawford, A. J., Cornford, S. L., Bevan, S. L., Zwinger, T.,
676 Gladstone, R., Alley, K., Pettit, E., and Bassis, J.: Rapid fragmentation of Thwaites Eastern Ice
677 Shelf, *The Cryosphere*, 16, 2545–2564, <https://doi.org/10.5194/tc-16-2545-2022>, 2022.
- 678 Brondex, J., Gagliardini, O., Gillet-Chaulet, F., and Durand, G.: Sensitivity of grounding line
679 dynamics to the choice of the friction law, *J. Glaciol.*, 63, 854–866,
680 <https://doi.org/10.1017/jog.2017.51>, 2017.
- 681 Brondex, J., Gillet-Chaulet, F., and Gagliardini, O.: Sensitivity of centennial mass loss projections
682 of the Amundsen basin to the friction law, *The Cryosphere*, 13, 177–195,
683 <https://doi.org/10.5194/tc-13-177-2019>, 2019.
- 684 Budd, W. F. and Jacka, T. H.: A review of ice rheology for ice sheet modelling, *Cold Reg. Sci.*

Technol., 16, 107–144, [https://doi.org/10.1016/0165-232X\(89\)90014-1](https://doi.org/10.1016/0165-232X(89)90014-1), 1989.

686 Budd, W. F., Keage, P. L., and Blundy, N. A.: Empirical Studies of Ice Sliding, *J. Glaciol.*, 23, 157–
687 170, <https://doi.org/10.3189/S0022143000029804>, 1979.

688 Burton-Johnson, A., Dziadek, R., and Martin, C.: Review article: Geothermal heat flow in
689 Antarctica: current and future directions, *The Cryosphere*, 14, 3843–3873,
690 <https://doi.org/10.5194/tc-14-3843-2020>, 2020.

691 Choi, Y., Seroussi, H., Morlighem, M., Schlegel, N.-J., and Gardner, A.: Impact of time-dependent
692 data assimilation on ice flow model initialization and projections: a case study of Kjer Glacier,
693 Greenland, *The Cryosphere*, 17, 5499–5517, <https://doi.org/10.5194/tc-17-5499-2023>, 2023.

694 Cornford, S. L., Martin, D. F., Payne, A. J., Ng, E. G., Le Brocq, A. M., Gladstone, R. M., Edwards,
695 T. L., Shannon, S. R., Agosta, C., Van Den Broeke, M. R., Hellmer, H. H., Krinner, G.,
696 Ligtenberg, S. R. M., Timmermann, R., and Vaughan, D. G.: Century-scale simulations of the
697 response of the West Antarctic Ice Sheet to a warming climate, *The Cryosphere*, 9, 1579–1600,
698 <https://doi.org/10.5194/tc-9-1579-2015>, 2015.

699 Dawson, E. J., Schroeder, D. M., Chu, W., Mantelli, E., and Seroussi, H.: Ice mass loss sensitivity
700 to the Antarctic ice sheet basal thermal state, *Nat. Commun.*, 13, 4957,
701 <https://doi.org/10.1038/s41467-022-32632-2>, 2022.

702 Dow, C.: Aurora Subglacial Basin GlaDs inputs, outputs and geophysical data, Zenodo [data set],
703 <https://doi.org/10.5281/zenodo.3525474>, 2019.

704 Dow, C. F., McCormack, F. S., Young, D. A., Greenbaum, J. S., Roberts, J. L., and Blankenship, D.
705 D.: Totten Glacier subglacial hydrology determined from geophysics and modeling, *Earth
706 Planet. Sci. Lett.*, 531, 115961, <https://doi.org/10.1016/j.epsl.2019.115961>, 2020.

707 Dziadek, R., Gohl, K., Diehl, A., and Kaul, N.: Geothermal heat flux in the Amundsen Sea sector
708 of West Antarctica: New insights from temperature measurements, depth to the bottom of the
709 magnetic source estimation, and thermal modeling, *Geochem. Geophys. Geosystems*, 18,
710 2657–2672, <https://doi.org/10.1002/2016GC006755>, 2017.

711 Fisher, A. T., Mankoff, K. D., Tulaczyk, S. M., Tyler, S. W., and Foley, N.: High geothermal heat
712 flux measured below the West Antarctic Ice Sheet, *Sci. Adv.*, 1(6), e1500093,
713 <https://doi.org/10.1126/sciadv.1500093>, 2015.

714 Fowler, A. C.: A theoretical treatment of the sliding of glaciers in the absence of cavitation, *Philos.
715 Trans. R. Soc. Lond. Ser. Math. Phys. Sci.*, 298, 637–681,
716 <https://doi.org/10.1098/rsta.1981.0003>, 1981.

717 Fujita, S. and Mae, S.: Strain in the ice sheet deduced from the crystal-orientation fabrics from bare
718 icefields adjacent to the Sør-Rondane Mountains, Dronning Maud Land, East Antarctica, *J.
719 Glaciol.*, 40, 135–139, <https://doi.org/10.3189/S0022143000003907>, 1994.

720 Gagliardini, O., Cohen, D., Råback, P., and Zwinger, T.: Finite-element modeling of subglacial
721 cavities and related friction law, *J. Geophys. Res. Earth Surf.*, 112, F02027,
722 <https://doi.org/10.1029/2006JF000576>, 2007.

723 Gerber, T. A., Lilien, D. A., Rathmann, N. M., Franke, S., Young, T. J., Valero-Delgado, F., Ershadi,
724 M. R., Drews, R., Zeising, O., Humbert, A., Stoll, N., Weikusat, I., Grinsted, A., Hvidberg, C.

725 S., Jansen, D., Miller, H., Helm, V., Steinhage, D., O'Neill, C., Paden, J., Gogineni, S. P., Dahl-
726 Jensen, D., and Eisen, O.: Crystal orientation fabric anisotropy causes directional hardening of
727 the Northeast Greenland Ice Stream, *Nat. Commun.*, 14, 2653, [https://doi.org/10.1038/s41467-](https://doi.org/10.1038/s41467-023-38139-8)
728 023-38139-8, 2023.

729 Gillet-Chaulet, F., Gagliardini, O., Seddik, H., Nodet, M., Durand, G., Ritz, C., Zwinger, T., Greve,
730 R., and Vaughan, D. G.: Greenland ice sheet contribution to sea-level rise from a new-
731 generation ice-sheet model, *The Cryosphere*, 6, 1561–1576, [https://doi.org/10.5194/tc-6-1561-](https://doi.org/10.5194/tc-6-1561-2012)
732 2012, 2012.

733 Gladstone, R., Schäfer, M., Zwinger, T., Gong, Y., Strozzi, T., Mottram, R., Boberg, F., and Moore,
734 J. C.: Importance of basal processes in simulations of a surging Svalbard outlet glacier, *The*
735 *Cryosphere*, 8, 1393–1405, <https://doi.org/10.5194/tc-8-1393-2014>, 2014.

736 Greenbaum, J. S., Blankenship, D. D., Young, D. A., Richter, T. G., Roberts, J. L., Aitken, A. R. A.,
737 Legresy, B., Schroeder, D. M., Warner, R. C., van Ommen, T. D., and Siegert, M. J.: Ocean
738 access to a cavity beneath Totten Glacier in East Antarctica, *Nat. Geosci.*, 8, 294–298,
739 <https://doi.org/10.1038/ngeo2388>, 2015.

740 Haeger, C., Petrunin, A. G., and Kaban, M. K.: Geothermal Heat Flow and Thermal Structure of the
741 Antarctic Lithosphere, *Geochem. Geophys. Geosystems*, 23, e2022GC010501,
742 <https://doi.org/10.1029/2022GC010501>, 2022.

743 Huang, Y., Zhao, L., Wolovick, M., Ma, Y., and Moore, J. C.: Using specularity content to evaluate
744 eight geothermal heat flow maps of Totten Glacier, *The Cryosphere*, 18, 103–119,
745 <https://doi.org/10.5194/tc-18-103-2024>, 2024.

746 Jordan, T. M., Martín, C., Brisbourne, A. M., Schroeder, D. M., and Smith, A. M.: Radar
747 Characterization of Ice Crystal Orientation Fabric and Anisotropic Viscosity Within an
748 Antarctic Ice Stream, *J. Geophys. Res. Earth Surf.*, 127, e2022JF006673,
749 <https://doi.org/10.1029/2022JF006673>, 2022.

750 Kamb, B.: Sliding motion of glaciers: Theory and observation, *Rev. Geophys.*, 8, 673–728,
751 <https://doi.org/10.1029/RG008i004p00673>, 1970.

752 Kang, H., Zhao, L., Wolovick, M., and Moore, J. C.: Evaluation of six geothermal heat flux maps
753 for the Antarctic Lambert–Amery glacial system, *The Cryosphere*, 16, 3619–3633,
754 <https://doi.org/10.5194/tc-16-3619-2022>, 2022.

755 Kim, B.-H., Seo, K.-W., Lee, C.-K., Kim, J.-S., Lee, W. S., Jin, E. K., and Van Den Broeke, M.:
756 Partitioning the drivers of Antarctic glacier mass balance (2003–2020) using satellite
757 observations and a regional climate model, *Proc. Natl. Acad. Sci.*, 121, e2322622121,
758 <https://doi.org/10.1073/pnas.2322622121>, 2024.

759 Larour, E., Seroussi, H., Morlighem, M., and Rignot, E.: Continental scale, high order, high spatial
760 resolution, ice sheet modeling using the Ice Sheet System Model (ISSM), *J. Geophys. Res.*,
761 117, F01022, <https://doi.org/10.1029/2011JF002140>, 2012.

762 Le Brocq, A. M., Payne, A. J., and Vieli, A.: An improved Antarctic dataset for high resolution
763 numerical ice sheet models (ALBMAP v1), *Earth Syst. Sci. Data*, 2, 247–260,
764 <https://doi.org/10.5194/essd-2-247-2010>, 2010.

- 765 Lipscomb, W. H., Leguy, G. R., Jourdain, N. C., Asay-Davis, X., Seroussi, H., and Nowicki, S.:
766 ISMIP6-based projections of ocean-forced Antarctic Ice Sheet evolution using the
767 Community Ice Sheet Model, *The Cryosphere*, 15, 633–661, [https://doi.org/10.5194/tc-15-](https://doi.org/10.5194/tc-15-633-2021)
768 633-2021, 2021.
- 769 Lhermitte, S., Sun, S., Shuman, C., Wouters, B., Pattyn, F., Wuite, J., Berthier, E., and Nagler, T.:
770 Damage accelerates ice shelf instability and mass loss in Amundsen Sea Embayment, *Proc.*
771 *Natl. Acad. Sci.*, 117, 24735–24741, <https://doi.org/10.1073/pnas.1912890117>, 2020.
- 772 Lösing, M. and Ebbing, J.: Predicting Geothermal Heat Flow in Antarctica With a Machine Learning
773 Approach, *J. Geophys. Res. Solid Earth*, 126, e2020JB021499,
774 <https://doi.org/10.1029/2020JB021499>, 2021.
- 775 MacAyeal, D. R.: A tutorial on the use of control methods in ice-sheet modeling, *J. Glaciol.*, 39, 91–
776 98, <https://doi.org/10.3189/S0022143000015744>, 1993.
- 777 Martín, C., Gudmundsson, G. H., Pritchard, H. D., and Gagliardini, O.: On the effects of anisotropic
778 rheology on ice flow, internal structure, and the age-depth relationship at ice divides, *J.*
779 *Geophys. Res. Earth Surf.*, 114, F04001, <https://doi.org/10.1029/2008JF001204>, 2009.
- 780 Martos, Y. M., Catalán, M., Jordan, T. A., Golynsky, A., Golynsky, D., Eagles, G., and Vaughan, D.
781 G.: Heat Flux Distribution of Antarctica Unveiled, *Geophys. Res. Lett.*, 44, 11,417–11,426,
782 <https://doi.org/10.1002/2017GL075609>, 2017.
- 783 Maule, C. F., Purucker, M. E., Olsen, N., and Mosegaard, K.: Heat Flux Anomalies in Antarctica
784 Revealed by Satellite Magnetic Data, *Science*, 309, 464–467,
785 <https://doi.org/10.1126/science.1106888>, 2005.
- 786 McCormack, F. S., Roberts, J. L., Dow, C. F., Stål, T., Halpin, J. A., Reading, A. M., and Siegert, M.
787 J.: Fine-Scale Geothermal Heat Flow in Antarctica Can Increase Simulated Subglacial Melt
788 Estimates, *Geophys. Res. Lett.*, 49, e2022GL098539, <https://doi.org/10.1029/2022GL098539>,
789 2022.
- 790 Morlighem, M., Seroussi, H., Larour, E., and Rignot, E.: Inversion of basal friction in Antarctica
791 using exact and incomplete adjoints of a higher-order model, *J. Geophys. Res. Earth Surf.*, 118,
792 1746–1753, <https://doi.org/10.1002/jgrf.20125>, 2013.
- 793 Morlighem, M., Rignot, E., Binder, T., Blankenship, D., Drews, R., Eagles, G., Eisen, O., Ferraccioli,
794 F., Forsberg, R., Fretwell, P., Goel, V., Greenbaum, J. S., Gudmundsson, H., Guo, J., Helm, V.,
795 Hofstede, C., Howat, I., Humbert, A., Jokat, W., Karlsson, N. B., Lee, W. S., Matsuoka, K.,
796 Millan, R., Mougintot, J., Paden, J., Pattyn, F., Roberts, J., Rosier, S., Ruppel, A., Seroussi, H.,
797 Smith, E. C., Steinhage, D., Sun, B., Broeke, M. R. V. D., Ommen, T. D. V., Wessem, M. V.,
798 and Young, D. A.: Deep glacial troughs and stabilizing ridges unveiled beneath the margins of
799 the Antarctic ice sheet, *Nat. Geosci.*, 13, 132–137, [https://doi.org/10.1038/s41561-019-0510-](https://doi.org/10.1038/s41561-019-0510-8)
800 8, 2020.
- 801 Nye, J. F.: Glacier sliding without cavitation in a linear viscous approximation, *Proc. R. Soc. Lond.*
802 *Math. Phys. Sci.*, 315, 381–403, <https://doi.org/10.1098/rspa.1970.0050>, 1970.
- 803 Park, I.-W., Jin, E. K., Morlighem, M., and Lee, K.-K.: Impact of boundary conditions on the
804 modeled thermal regime of the Antarctic ice sheet, *The Cryosphere*, 18, 1139–1155,

805 <https://doi.org/10.5194/tc-18-1139-2024>, 2024.

806 Paterson, W. S. B.: Why ice-age ice is sometimes “soft,” *Cold Reg. Sci. Technol.*, 20, 75–98,
807 [https://doi.org/10.1016/0165-232X\(91\)90058-O](https://doi.org/10.1016/0165-232X(91)90058-O), 1991.

808 Pattyn, F.: Sea-level response to melting of Antarctic ice shelves on multi-centennial timescales
809 with the fast Elementary Thermomechanical Ice Sheet model (f.ETISh v1.0), *The*
810 *Cryosphere*, 11, 1851–1878, <https://doi.org/10.5194/tc-11-1851-2017>, 2017.

811 Payne, A. J., Nowicki, S., Abe-Ouchi, A., Agosta, C., Alexander, P., Albrecht, T., Asay-Davis, X.,
812 Aschwanden, A., Barthel, A., Bracegirdle, T. J., Calov, R., Chambers, C., Choi, Y., Cullather,
813 R., Cuzzone, J., Dumas, C., Edwards, T. L., Felikson, D., Fettweis, X., Galton-Fenzi, B. K.,
814 Goelzer, H., Gladstone, R., Golledge, N. R., Gregory, J. M., Greve, R., Hattermann, T.,
815 Hoffman, M. J., Humbert, A., Huybrechts, P., Jourdain, N. C., Kleiner, T., Munneke, P. K.,
816 Larour, E., Le Clec’H, S., Lee, V., Leguy, G., Lipscomb, W. H., Little, C. M., Lowry, D. P.,
817 Morlighem, M., Nias, I., Pattyn, F., Pelle, T., Price, S. F., Quiquet, A., Reese, R., Rückamp, M.,
818 Schlegel, N., Seroussi, H., Shepherd, A., Simon, E., Slater, D., Smith, R. S., Straneo, F., Sun,
819 S., Tarasov, L., Trusel, L. D., Van Breedam, J., Van De Wal, R., Van Den Broeke, M.,
820 Winkelmann, R., Zhao, C., Zhang, T., and Zwinger, T.: Future Sea Level Change Under
821 Coupled Model Intercomparison Project Phase 5 and Phase 6 Scenarios From the Greenland
822 and Antarctic Ice Sheets, *Geophys. Res. Lett.*, 48, e2020GL091741,
823 <https://doi.org/10.1029/2020GL091741>, 2021.

824 Peyaud, V., Bouchayer, C., Gagliardini, O., Vincent, C., Gillet-Chaulet, F., Six, D., and Laarman,
825 O.: Numerical modeling of the dynamics of the Mer de Glace glacier, French Alps: comparison
826 with past observations and forecasting of near-future evolution, *The Cryosphere*, 14, 3979–
827 3994, <https://doi.org/10.5194/tc-14-3979-2020>, 2020.

828 Pittard, M. L., Roberts, J. L., Galton-Fenzi, B. K., and Watson, C. S.: Sensitivity of the Lambert-
829 Amery glacial system to geothermal heat flux, *Ann. Glaciol.*, 57, 56 – 68,
830 <https://doi.org/10.1017/aog.2016.26>, 2016.

831 Pollard, D. and DeConto, R. M.: A simple inverse method for the distribution of basal sliding
832 coefficients under ice sheets, applied to Antarctica, *The Cryosphere*, 6, 953–971,
833 <https://doi.org/10.5194/tc-6-953-2012>, 2012.

834 Pritchard, H. D., Arthern, R. J., Vaughan, D. G., and Edwards, L. A.: Extensive dynamic thinning
835 on the margins of the Greenland and Antarctic ice sheets, *Nature*, 461, 971–975,
836 <https://doi.org/10.1038/nature08471>, 2009.

837 Pritchard, H.D., Fretwell, P.T., Fremand, A.C. et al. Bedmap3 updated ice bed, surface and thickness
838 gridded datasets for Antarctica. *Sci Data* 12, 414 (2025). [https://doi.org/10.1038/s41597-025-](https://doi.org/10.1038/s41597-025-04672-y)
839 [04672-y](https://doi.org/10.1038/s41597-025-04672-y)

840 Purucker, M.: Geothermal heat flux data set based on low resolution observations collected by the
841 CHAMP satellite between 2000 and 2010, and produced from the MF-6 model following the
842 technique described in Fox Maule et al. (2005), Interactive System for Ice sheet Simulation
843 [data set], https://core2.gsfc.nasa.gov/research/purucker/heatflux_mf7_foxmaule05.txt ~~(last~~
844 ~~access: 24 December 2023)~~, 2012.

845 Rathmann, N. M. and Lilien, D. A.: Inferred basal friction and mass flux affected by crystal-
846 orientation fabrics, *J. Glaciol.*, 68, 236–252, <https://doi.org/10.1017/jog.2021.88>, 2022.

847 Reading, A. M.: Antarctic geothermal heat flow and its implications for tectonics and ice sheets,
848 *Nat. Rev. Earth Environ.*, 3, 814–831, <https://doi.org/10.1038/s43017-022-00348-y>, 2022.

849 Reese, R., Garbe, J., Hill, E. A., Urruty, B., Naughten, K. A., Gagliardini, O., Durand, G., Gillet-
850 Chaulet, F., Gudmundsson, G. H., Chandler, D., Langebroek, P. M., and Winkelmann, R.: The
851 stability of present-day Antarctic grounding lines – Part 2: Onset of irreversible retreat of
852 Amundsen Sea glaciers under current climate on centennial timescales cannot be excluded,
853 *The Cryosphere*, 17, 3761–3783, <https://doi.org/10.5194/tc-17-3761-2023>, 2023.

854 Ross, N., Bingham, R. G., Corr, H. F. J., Ferraccioli, F., Jordan, T. A., Le Brocq, A., Rippin, D. M.,
855 Young, D., Blankenship, D. D., and Siegert, M. J.: Steep reverse bed slope at the grounding
856 line of the Weddell Sea sector in West Antarctica, *Nat. Geosci.*, 5, 393–396,
857 <https://doi.org/10.1038/ngeo1468>, 2012.

858 Robel, A. A., Schoof, C., and Tziperman, E.: Rapid grounding line migration induced by internal
859 ice stream variability, *J. Geophys. Res. Earth Surf.*, 119, 2430–2447,
860 <https://doi.org/10.1002/2014JF003251>, 2014.

861 Rignot, E., Mouginot, J., and Scheuchl, B.: MEaSURES InSAR-Based Antarctica Ice Velocity Map,
862 Version 2, Boulder, Colorado USA, NASA National Snow and Ice Data Center Distributed
863 Active Archive Center [data Set], <https://doi.org/10.5067/D7GK8F5J8M8R>, 2017.

864 Rignot, E., Mouginot, J., Scheuchl, B., Van Den Broeke, M., Van Wessem, M. J., and Morlighem,
865 M.: Four decades of Antarctic Ice Sheet mass balance from 1979–2017, *Proc. Natl. Acad. Sci.*,
866 116, 1095–1103, <https://doi.org/10.1073/pnas.1812883116>, 2019.

867 Schannwell, C., Drews, R., Ehlers, T. A., Eisen, O., Mayer, C., Malinen, M., Smith, E. C., and
868 Eisermann, H.: Quantifying the effect of ocean bed properties on ice sheet geometry over 40
869 000 years with a full-Stokes model, *The Cryosphere*, 14, 3917–3934,
870 <https://doi.org/10.5194/tc-14-3917-2020>, 2020.

871 Schoof, C.: On the mechanics of ice-stream shear margins, *J. Glaciol.*, 50, 208–218,
872 <https://doi.org/10.3189/172756504781830024>, 2004.

873 Schoof, C.: The effect of cavitation on glacier sliding, *Proc. R. Soc. Math. Phys. Eng. Sci.*, 461,
874 609–627, <https://doi.org/10.1098/rspa.2004.1350>, 2005.

875 Schroeder, D. M., Blankenship, D. D., and Young, D. A.: Evidence for a water system transition
876 beneath Thwaites Glacier, West Antarctica, *Proc. Natl. Acad. Sci.*, 110, 12225–12228,
877 <https://doi.org/10.1073/pnas.1302828110>, 2013.

878 Seroussi, H., Nowicki, S., Simon, E., Abe-Ouchi, A., Albrecht, T., Brondex, J., Cornford, S., Dumas,
879 C., Gillet-Chaulet, F., Goelzer, H., Gолledge, N. R., Gregory, J. M., Greve, R., Hoffman, M. J.,
880 Humbert, A., Huybrechts, P., Kleiner, T., Larour, E., Leguy, G., Lipscomb, W. H., Lowry, D.,
881 Mengel, M., Morlighem, M., Pattyn, F., Payne, A. J., Pollard, D., Price, S. F., Quiquet, A.,
882 Reerink, T. J., Reese, R., Rodehacke, C. B., Schlegel, N.-J., Shepherd, A., Sun, S., Sutter, J.,
883 Van Breedam, J., Van De Wal, R. S. W., Winkelmann, R., and Zhang, T.: initMIP-Antarctica:
884 an ice sheet model initialization experiment of ISMIP6, *The Cryosphere*, 13, 1441–1471,

885 <https://doi.org/10.5194/tc-13-1441-2019>, 2019.

886 Shackleton, C., Matsuoka, K., Moholdt, G., Van Liefferinge, B., and Paden, J.: Stochastic
887 Simulations of Bed Topography Constrain Geothermal Heat Flow and Subglacial Drainage
888 Near Dome Fuji, East Antarctica, *J. Geophys. Res. Earth Surf.*, 128, e2023JF007269,
889 <https://doi.org/10.1029/2023JF007269>, 2023.

890 Shapiro, N.: Inferring surface heat flux distributions guided by a global seismic model: particular
891 application to Antarctica, *Earth Planet. Sci. Lett.*, 223, 213–224,
892 <https://doi.org/10.1016/j.epsl.2004.04.011>, 2004.

893 Shen, W., Wiens, D. A., Lloyd, A. J., and Nyblade, A. A.: A Geothermal Heat Flux Map of Antarctica
894 Empirically Constrained by Seismic Structure, *Geophys. Res. Lett.*, 47, e2020GL086955,
895 <https://doi.org/10.1029/2020GL086955>, 2020.

896 Siahhaan, A., Smith, R. S., Holland, P. R., Jenkins, A., Gregory, J. M., Lee, V., Mathiot, P., Payne, A.
897 J., Ridley, J. K., and Jones, C. G.: The Antarctic contribution to 21st-century sea-level rise
898 predicted by the UK Earth System Model with an interactive ice sheet, *The Cryosphere*, 16,
899 4053 – 4086, <https://doi.org/10.5194/tc-16-4053-2022>, 2022.

900 Smith-Johnsen, S., Schlegel, N. -J., De Fleurian, B., and Nisancioglu, K. H.: Sensitivity of the
901 Northeast Greenland Ice Stream to Geothermal Heat, *J. Geophys. Res. Earth Surf.*, 125,
902 e2019JF005252, <https://doi.org/10.1029/2019JF005252>, 2020.

903 Stål, T., Reading, A. M., Halpin, J. A., and Whittaker, J. M.: Antarctic Geothermal Heat Flow Model:
904 Aq1, *Geochem. Geophys. Geosystems*, 22, e2020GC009428,
905 <https://doi.org/10.1029/2020GC009428>, 2021.

906 Sun, S., Cornford, S. L., Moore, J. C., Gladstone, R., and Zhao, L.: Ice shelf fracture
907 parameterization in an ice sheet model, *The Cryosphere*, 11, 2543–2554,
908 <https://doi.org/10.5194/tc-11-2543-2017>, 2017.

909 Tsai, V. C., Stewart, A. L., and Thompson, A. F.: Marine ice-sheet profiles and stability under
910 Coulomb basal conditions, *J. Glaciol.*, 61, 205–215, <https://doi.org/10.3189/2015JoG14J221>,
911 2015.

912 Van Liefferinge, B., Pattyn, F., Cavitte, M. G. P., Karlsson, N. B., Young, D. A., Sutter, J., and Eisen,
913 O.: Promising Oldest Ice sites in East Antarctica based on thermodynamical modelling, *The*
914 *Cryosphere*, 12, 2773–2787, <https://doi.org/10.5194/tc-12-2773-2018>, 2018.

915 Weertman, J.: On the Sliding of Glaciers, *J. Glaciol.*, 3, 33–38,
916 <https://doi.org/10.3189/S0022143000024709>, 1957.

917 Young, D. A., Schroeder, D. M., Blankenship, D. D., Kempf, S. D., and Quartini, E.: The distribution
918 of basal water between Antarctic subglacial lakes from radar sounding, *Philos. Trans. R. Soc.*
919 *Math. Phys. Eng. Sci.*, 374, 20140297, <https://doi.org/10.1098/rsta.2014.0297>, 2016.

920 Zhao, L., Moore, J. C., Sun, B., Tang, X., and Guo, X.: Where is the 1-million-year-old ice at Dome
921 A?, *The Cryosphere*, 12, 1651–1663, <https://doi.org/10.5194/tc-12-1651-2018>, 2018.

922 [Zhao, L., Wolovick, M., Huang, Y., Moore, J. C. and Ma, Y.: Totten Glacier Thermal Structure,](#)
923 [Zenodo \[data set\], https://doi.org/10.5281/zenodo.7825456, 2023.](https://doi.org/10.5281/zenodo.7825456)

924 [Zhang, X.: Near-surface air temperature data of Antarctic ice sheet \(2001-2018\), National Tibetan](#)

925 [Plateau / Third Pole Environment Data Center \[data set\],](#)
926 <https://doi.org/10.11888/Atmos.tpsc.272234>, 2022.
927 Zhang, X., Dong, X., Zeng, J, Hou, S., Smeets, P., Reijmer, C. H., and Wang, Y., Spatiotemporal
928 Reconstruction of Antarctic Near-Surface Air Temperature from MODIS Observations, *J.*
929 *Clim.*, 35, 5537-5553, 2022.
930 Zwinger, T., Schäfer, M., Martín, C., and Moore, J. C.: Influence of anisotropy on velocity and age
931 distribution at Scharffenbergbotnen blue ice area, *The Cryosphere*, 8, 607–621,
932 <https://doi.org/10.5194/tc-8-607-2014>, 2014.
933